University of Wisconsin Milwaukee

UWM Digital Commons

August 2020

Development of an Advanced Zinc Air Flow Battery System (Phase 2)

Jingyu Si
University of Wisconsin-Milwaukee

DEVELOPMENT OF AN ADVANCED

ZINC AIR FLOW BATTERY SYSTEM (PHASE 2)

by

Jingyu Si

A Dissertation Submitted in

Partial Fulfillment of the

Requirements for the Degree of

Doctor of Philosophy

in Engineering

at

University of Wisconsin-Milwaukee

August 2020

ABSTRACT

DEVELOPMENT OF AN ADVANCED
ZINC AIR FLOW BATTERY SYSTEM (PHASE 2)

by

Jingyu Si

The University of Wisconsin-Milwaukee, 2020
Under the Supervision of Professor Deyang Qu

A zinc-air battery is the promising energy storage technology for large-scale energy storage applications due to its low cost, environmental friendliness, and high energy density. However, the electrically rechargeable zinc−air batteries suffer from poor energy efficiency and cycle life because of critical problems such as passivation, dendrite growth, and hydrogen evolution reaction.   The proliferation of zinc−air batteries is limited.

The zinc-air flow battery combines the advantages of both a zinc-air battery and a redox flow battery. This combination permits the zinc-air flow battery to compete with the current leading battery technologies in the marketplace. A rechargeable Zn-air flow battery with an automatic control system was designed and prototyped in our previous researches.

In this study, the engineering aspects of the Zn-air flow battery system have been investigated. The reactor was re-designed and optimized. The non-reacted "dead zinc" problems and the deformation of the air cathode were solved in the Gen 2 design. The reactor's electrochemical performance was tripled, which benefited from applying the additive manufacturing processes (3D print) in the mechanical design. The air cathode fabrication process parameters were investigated, including the thickness, the binder content, and the

expanded graphite content of the active layer. The 0.2mm was chosen as the desired thickness considering the efficiency of material and the fabrication's easiness. The PTFE content was determined as 5%, and expanded graphite content was 10% in the active layer for the balance of the electronic conductivity and tenacity. The LabVIEW based battery management system build-up and control algorithm was discussed.

TABLE OF CONTENTS

LIST OF FIGURES

LIST OF TABLES

LIST OF ABBREVIATIONS

3D	three-dimensional
2D	two-dimensional
AC	alternating current
AM	additive-manufacturing
BMS	battery management system
CAD	computer aid-design
CNC	computerized numerical control
DoD	depth-of-discharge
EES	electrical energy storage
EIS	electrochemical impedance spectroscopy
EPD	electrophoretic deposition
EV	electrical vehicle
GDE	gas diffusion electrode
GDL	gas diffusion layer
ICE	internal combustion engine
I/O	input/output
IR	current * resistance
LFP	Lithium iron phosphate battery
LIB	Lithium-ion batteries
LabVIEW	Laboratory Virtual Instrument Engineering Workbench

MEA	membrane electrode assembly
NHE	Normal Hydrogen Electrode
NI	National Instruments
OER	oxygen-evolution reaction
ORR	oxygen-reduction reaction
PEIS	potentiodynamic electrochemical impedance spectroscopy
PID	proportional–integral–derivative
PTFE	Polytetrafluoroethylene
PVC	Polyvinyl chloride
PWA	acid washed powdered activated carbon
RFB	redox flow battery
SLA	stereolithography
SLM	selective laser melting
SLS	selective laser sintering
VI	virtual instruments
VRFB	Vanadium redox flow battery

ACKNOWLEDGEMENTS

I want to express my sincere appreciation and gratitude to my advisor, Deyang Qu, for his patient guidance, support, and mentorship throughout my studies at UW-Milwaukee. His profound knowledge and encouragement have made my Ph.D. study learning and thought and experience. I'm truly fortunate to work on research together with him.

I would also like to thank my committee members, Professor Junhong Chen, Professor Benjamin Church, Professor Yongjin Sung, Professor Shama Mirza, and Professor Jorg Woehl, for serving on my doctoral committee. Their kind guidance, thought-provoking suggestions have helped me complete my dissertation successfully.

I want to give special thanks to Dr. Dong Zheng, Dr. GongWei Wang, Prof. Dan Liu, Dr. Joshua Harris, Robert Dahl, and Hayley Sentz in the UWM Mechanical department for their everyday experiment assistance. Professor H.A. Owen from the UWM Biology department for her guidance on SEM imaging. John Condon and Michael Powley in CEAS Student Machine Shop for their prototyping and machining. Their valuable input has led this more research insights into this work.

I am grateful to my dear colleagues and friends for sharing the time at UW-Milwaukee. Mainly, I'd like to thank Tianyao Ding, Xiaoxiao Zhang, Huannan Qu, for their encouragement and assistance in work.

Finally, I would like to express my most significant appreciation to my parents for their unconditional love and support to me in this beautiful journey.

Chapter 1 Introduction of thesis

1.1 Research Motivation

The global electrical vehicle (E.V.) industry continues to ramp up since Tesla announced its mass production of all-electric car model S in 2012. Model S quickly becomes a top-selling all-electric car worldwide.   More than 1.18 million electric vehicles are now on the road in the U.S (Figure 1.1) [1].There are 46 models of all-electrical vehicles available on the market from different manufactures [2], and around 400 new models are expected to be launched by 2023 [3]. All the traditional automakers are now jumped onto the EV bandwagon of EV, to compete with the new technology competitors in this merging market. For example, Daimler has stopped developing internal combustion engines and focused on electric cars.   Nine countries have announced they will phase out internal combustion engine (ICE) vehicles starting from 2030 to 2050. The EV will be dominant in the next couple of decades.
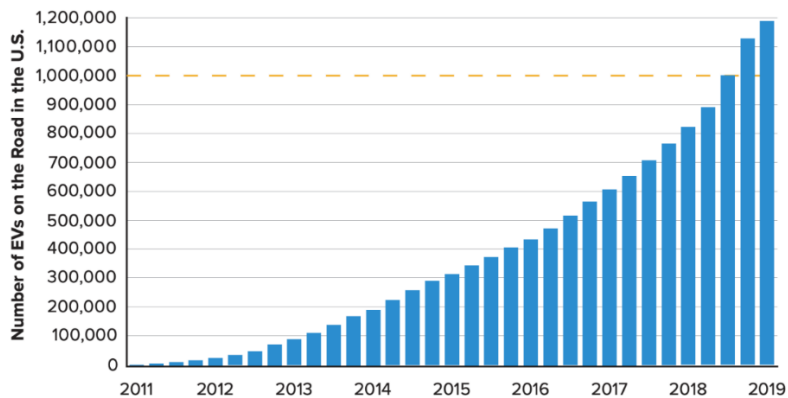
Figure 1.1 Number of EVs on the Road in the U.S.[1]

According to Statista, there are 272.5 million vehicles in operation in the United States by 2017. The average energy consumption of an EV on the market is 297 Wh per mile [2], and the average miles driven per year is 13,476 miles [4]. Assuming EVs replaced all the United States vehicles, the electrical consumption would be about 1091 billion kWh per year. According to the U.S. Energy Information Administration numbers, 4171 billion kWh of electricity were generated at the utility-scale electricity generation facilities in the United States in 2018.

The infrastructures of power generation need to be to satisfy the significant increase in the consumption of electric energy.   One of the problems of the existing electricity generation is over-designed and expensive power plants. [5] The conventional electricity-generating industries are carrying capacity dependent. They are designed based on the estimation of peak demands. However, the electricity demand could vary based on many factors, for example, weather, day, night, and unpredicted events. The carefully designed peak demand may only be needed for a very short time each year. Such inefficient designs resulted from no adequate energy storage facility in a conventional power plant to smooth a variation and buffer sudden changes. Electricity has to be transformed and distributed to consumers from remote and large power plants, once it is generated. Gigawatts of electricity generated from hydro or wind turbines may stay idle during non-peak hours, while insufficient energy may be produced to meet the need during peak hours.   An electrical energy storage (EES) could be one of the solutions to this issue. The EES makes it possible to decouple the peak demand and the designed capacity of power plants. For example, a 10 MW power plant could deliver 12 MW electricity for 5 hours with 10 MWh EES. It will provide more flexibility to a power plant designer and improve the efficiency of electricity-generating.

Another issue of conventional electricity-generating industries is on the massive consumption of fossil fuels. According to the U.S. Energy Information Administration in 2018, 63.6% of the

total electricity in the U.S. was still generated from fossil fuels (coal, natural gas, and petroleum) and only 16.9% (703 billion kWh) the electricity was from renewable sources. [6]. The EVs are still mostly powered by fossil fuels since most of the electricity is generated from fossil fuels. The efficiency of using fossil fuel conversion has been improved substantially, and the ultimate goal is to use renewable energy eventually. One of the significant benefits of replacing fossil fuels with renewable energy is reducing greenhouse gases, such as CO_2, which exceeds 400 ppm in the atmosphere. [7]

There are many obstacles to merge the renewable energy production in a traditional electricity grid. One is to avoid destabilizing the exiting national electrical grid. [8]. The production rate of the energy generated from renewable sources is at the mercy of mother nature. For example, any blockage of sun or wind can significantly cause a reduction of the energy generation from photovoltaics and wind turbines in a very short time. Such sudden and unpredictable giant swing of energy output will impose massive stress on a national electricity network. There is also a considerable gap between the peak and base periods of renewable energy sources. One the other hand, the electricity supply needs to flexible to suit the change of demand. For example, the demand could significantly increase in 1h just because everybody goes back to home and turns on air conditioners. Merging renewable energy into an existing electrical grid is a challenge. The EES could be used as a buffer to interface renewable energy with an electrical grid. The EES can store the energy at the period of a high energy generation or a low energy demand, and then release the stored energy when needed. [5] This will fill the gap and prevent the giant energy swing. EES is indispensable for energy management, frequency regulation, peak shaving, load leveling, seasonal storage, and standby generation during a fault. [9]

Various ESS technologies have been developed with different stages of maturity and scales of

capacity. Pumped hydroelectric systems (e.g., 169 GW) count for 96% of the world's total installed storage capacity. while 3.2 GW of thermal, 1.57 GW of electro-mechnical, 1.63 GW of electrochemical and 15 GW of Hydrogenin 2017 [10]

The electrochemical EES is the third most developed ESS technology for global power storage capacity. And because of the high-energy convention efficiency, versatility, and scalability, batteries are becoming the most promising ESS applications candidate.

Battery and supercapacitor are the two major types of electrochemical ESS technologies. They are applied in different time domains. A supercapacitor is the electrical/electrochemical energy storage systems that can be used under the conditions in which the electrical power output is highly time-dependent.

While conventional battery systems can be considered lower power devices, the energy density for a traditional battery is much higher than a supercapacitor. The energy density of various batteries is tabulated in table 1-1 and illustrated in Figure 1.2. The power-energy relation of various energy storage devices is also presented in Figure 1.3.

Battery type	Electrochemical reaction	Theoretical energy density (Wh Kg^{-1})	The advantages and disadvantages
Li-Air	Discharge: $2Li^+ + O_2 + 2e^- \rightarrow Li_2O_2$ (Cathode); $2Li \rightarrow 2Li+ + 2e$ (Anode)	5217	Advantages: Super high energy density
	Charge: $Li_2O_2 \rightarrow 2Li+ + O_2 + 2e^-$ (Cathode); $2Li^+ + 2e^- \rightarrow 2Li$ (Anode)		Disadvantages: No practical applications so far
Li-S	Discharge: $S + 2Li^+ + 2e^- \rightarrow Li_2S$ (Cathode); $2Li \rightarrow 2Li + 2e^-$ (Anode)	2654	Advantages: Super high energy density
	Charge: $Li_2S \rightarrow S + 2Li^+ + 2e^-$ (Cathode); $2Li + 2e^- \rightarrow 2Li$ (Anode)		Disadvantages: No practical applications so far
Zn-Air	Discharge: $\frac{1}{2} O_2 + H_2O + 2e^- \rightarrow 2OH^-$ (Cathode)	1094	Advantages: Low cost

	Zn + 4OH$^-$→ ZnO + H$_2$O + 2OH$^-$+ 2e$^-$ (Anode)		Low safety risk
	Charge: 2OH$^-$→ ½ O$_2$ + H$_2$O + 2e$^-$ (Cathode) Zn + 4OH$^-$→ ZnO + H$_2$O + 2OH$^-$+ 2e$^-$ (Anode)		Disadvantages: Poor rechargeability Low utilization of the anode
Li-ion	Discharge: Li$_{1-x}$MO$_2$ + xLi$^+$ + xe$^-$→ LiMO$_2$ (Cathode) Li$_x$C$_6$ → xLi$^+$ + xe$^-$ + 6C (Anode)	360	Advantages: High voltage Long cycling life High efficiency Quick charge and discharge
	Charge: LiMO$_2$→ Li$_{1-x}$MO$_2$ + xLi$^+$ + xe$^-$ (Cathode) xLi$^+$ + xe$^-$ + 6C → Li$_x$C$_6$ (Anode)		Disadvantages: High cost High flammability
Ni-MxH	Discharge: M + H$_2$O + e$^-$ → MH + OH$^-$ (Cathode) Ni(OH)$_2$ + OH$^-$ → NiO(OH) + H$_2$O + e$^-$ (Anode)	240	Advantages: Longer cycling life Better load performance comparing with lead-acid
	Charge: MH + OH$^-$ →M + H$_2$O + e$^-$ (Cathode) NiO(OH) + H$_2$O + e$^-$ → Ni(OH)$_2$ + OH$^-$ (Anode)		Disadvantages: Environment issue with Cd Memory effect
Lead-Acid	Discharge: PbO$_2$(s) + HSO$_4$$^-$(aq) + 3H$^+$(aq) + 2e$^-$ → PbSO$_4$(s) + 2H$_2$O(l) (Cathode); Pb(s) + HSO$_4$$^-$(aq) → PbSO$_4$(s) + H$^+$(aq) + 2e$^-$ (Anode)	171	Advantages: Fast response times Low self-discharge rates Low cost High currents supply
	Charge: PbSO$_4$(s) + 2H$_2$O(l) → PbO$_2$(s) + HSO$_4$$^-$(aq) + 3H+(aq) + 2e$^-$ (Cathode); Pb(s) + HSO$_4$$^-$(aq) → PbSO$_4$(s) + H$^+$(aq) + 2e$^-$ (Anode)		Disadvantages: Low cycling life Low operational lifetime

Table 1-1 Summary of several types of rechargeable batteries [11]
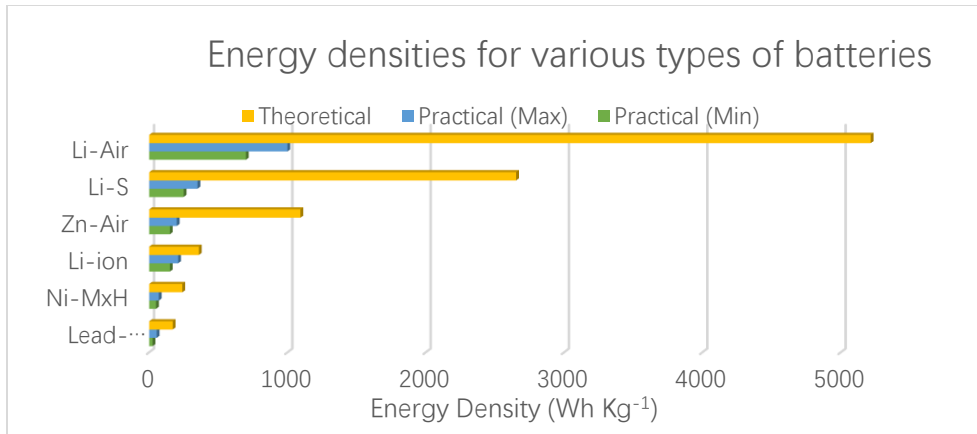
Figure 1.2 Comparison of energy density for different types of rechargeable batteries [11]
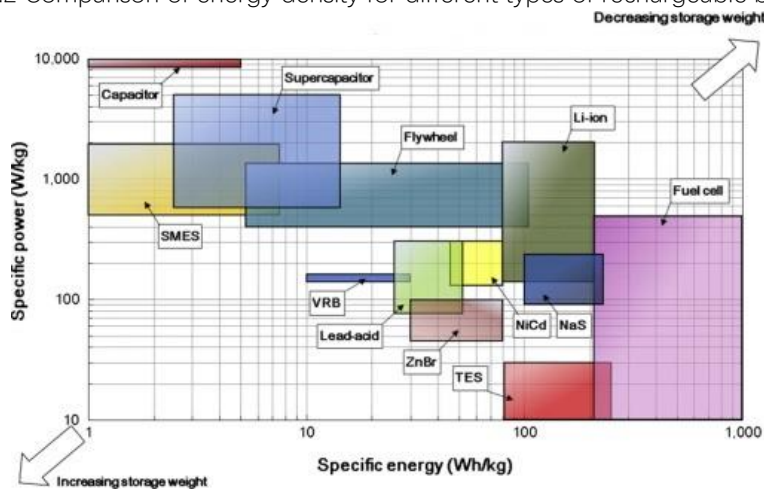
Figure 1.3 Comparison of specific energy and specific power. [11]

1.2 Progressive of research

In our phase 1 study, a Zn-air flow battery prototype with an automatic was designed and fabricated [11]. The Zn-air flow battery inherited the advantages of two electrochemical systems and overcame the respective limits. The zinc particles suspended in an alkaline gel electrolyte flow through a storage tank housing and a discharge unit. The flow speed was controlled in such a way that the depth-of-discharge (DoD) of Zn remained constant. The electric load fluctuation was controlled by the Zn resident time in the discharge unit. This novel design could minimize the shape change of the zinc particles to the greatest extent to ensure smooth flow and prevent the clog of the cell system., The major advantages of a Zn-air flow cell are the significantly increase of energy density, the decreases of cost and environmental benign in comparison with a state-of-art Vanadium redox flow battery (VRFB)

The previous study mainly focused on proof of concept and electrochemical studies of the system. Phase 2 studies were concentrated on the engineering aspects of optimizing, evolution, and problem-solving. The reactor design, air cathode fabrication, and control algorithm implementation were discussed in this thesis.

Chapter 2 Literature review

2.1 Introduction

Metal air batteries and redox flow batteries are the two kinds of electrochemical systems that could suit the requirements of a large scale of EES applications. They are all low cost and long-lasting systems.   Various redox couples could be applied in those two electrochemical systems. They are discussed in 2.2 and 2.3. The zinc-air and rechargeable zinc-air battery are discussed in 2.4.

Transforming the electrochemical theory to mature ESS applications is challenging because the ESS device's design and fabrication are also critical factors. The conventional subtractive manufacturing technique, like CNC machinery, plays a vital role in the current battery industry. For example, the fabrication of the case and the current collector of the batteries. The new demand, like EV, requires lower prices and more energy of each signal battery. Discovering new low-cost material is one path to fulfill the target and optimizing the design and fabrication process provides another route to get there. The additive-manufacturing (AM) technique, known as 3D-printing, provides a brand-new platform for the rapid design and fabrication of ESS devices. It will be introduced in 2.5

All the electrochemical EES devices are operated under certain conditions to avoid irreversible damages to the system. For example, an overcharge or an over discharge of a battery could result in the degradation of battery life and even a catastrophic event like fire as in the case of Li-ion batteries. Thus, adequate external control is necessary to maintain the EES devices under self-

operation conditions, the battery management system (BMS) is introduced in 2.6

2.2 Metal air batteries

The Lead-Acid batteries (LAB) and Lithium-ion batteries (LIB) are widely used in the W-scale EES like UPS and the kW-scale EES like EVs. The energy density of LIBs has been incrementally increasing while the cost has been reduced since the first announcement in 1991 by Sony. LABs are now gradually replaced by the LIBs in the area of EES. The high cost, high maintenance, low durability and safety impede the application of either LABs or LIBs in the MW and GW EES arenas. For example, the kW-scale application, like Tesla model 3 has a battery pack made up of thousands of 21700 form of Li-ion cells. A grid-scale ESS is normal at MW-scale, which would need millions of individual LIB cells. The battery management system for millions of individual cells is quite a challenge for current electrical and computing technology. Moreover, the large number of cells also exponentially increases the complexity and the possibility of system failure. Metal air batteries have attracted a lot of attention recently.

A metal-air battery has compelling energy density (either capacity-to-volume or capacity-to-mass) because only anode active material stores in the battery container, the unlimited supply of the cathode active material (oxygen) is from the atmosphere.

The oxygen-reduction reaction (ORR) and oxygen-evolution reaction (OER) are two essential reactions on the cathode during the discharge and recharge, respectively. Based on the anode materials, lithium-air (Li-air), sodium-air (Na-air), potassium-air (K-air), zinc-air (Zn-air), iron-air (Fe-air), magnesium-air (Mg-air), and aluminum-air (Al-air) batteries are under investigation. [12] Figure 2.1 shows the comparison of the energy density of different metal-air systems.
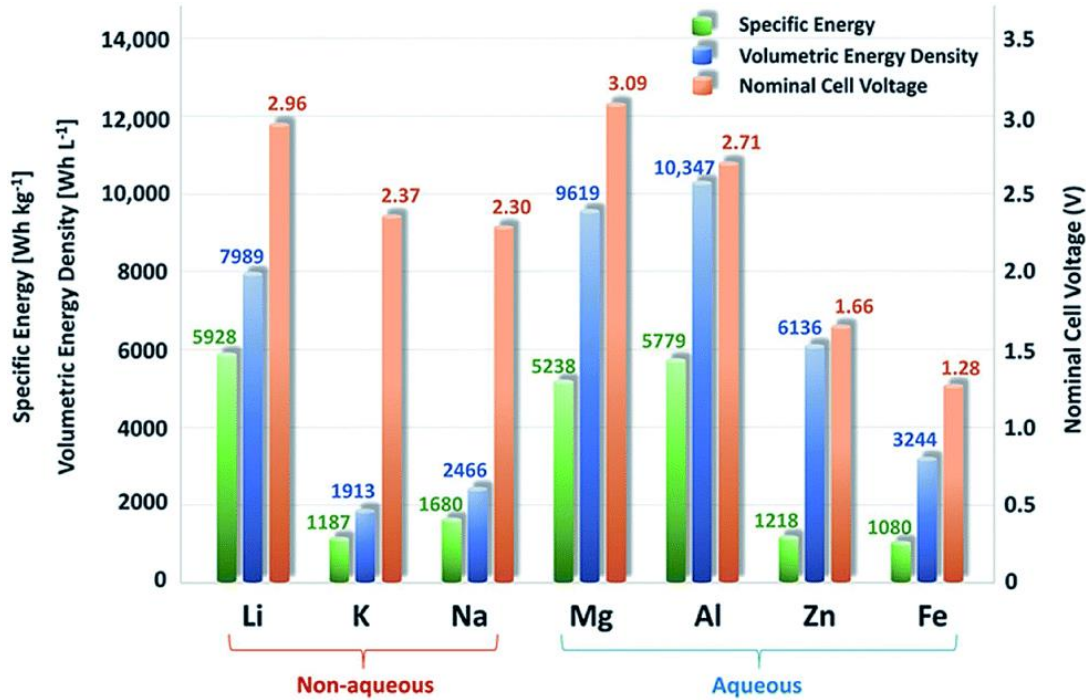
Figure 2.1   Theoretical specific/volumetric energy densities and nominal cell voltages for various metal–air batteries [13]

Li, Na and K are alkali metals, they can only work in a non-aqueous electrolyte. While Mg, Al, Zn and Fe may work in both aqueous and non-aqueous electrolytes. The fundamental electrochemical reactions at the anode in an aqueous and a non-aqueous are distinct.

An aqueous electrolyte is commonly used in a metal-air battery.   During the discharge reaction, the metallic anode is oxidized, the metal cations combine with hydroxide ions (OH⁻) forming metal hydroxides (eq1).   In a parallel side reaction, the active metal may also react with water. H_2 gas is generated. The undesired parasitic reaction is responsible for the self-discharge. At the air cathode, the O_2 molecules from the atmosphere diffuse through the porous gas diffusion layer (GDL) of a gas diffusion electrode and are reduced to hydroxide ions (OH⁻) on the catalyst layer of the GDL.[14] This is a typical oxygen reduction reaction (ORR) in alkaline electrolyte. In the electrolyte solution, the hydroxide ions (OH⁻) are soluble and move away from the cathode to the anode.

The anode reaction: $M + xOH^- \rightarrow M(OH)_x + xe^-$ (1)

The cathode reaction: $$O_2 + 4e^- + 2H_2O \rightarrow 4OH^- \tag{2}$$

The overall reaction: $$4M + xO_2 + 2xH_2O \rightarrow 4M(OH)_x \tag{3}$$

Undesired parasitic reaction $$2M + 2xH_2O \rightarrow 2M(OH)_x + xH_2 \tag{4}$$
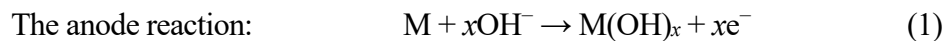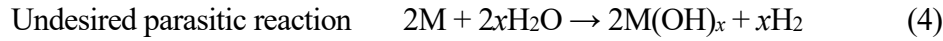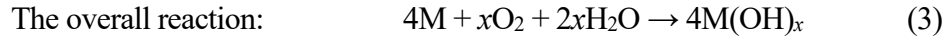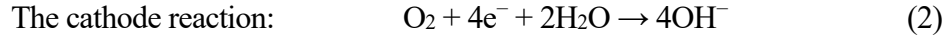
In a non-aqueous metal-air cell, the oxides formed by reducing O_2 could react with the metal ions from the anode oxidation, a non-soluble metal oxide precipitate will be formed. The overall reaction can be written as reaction 8. [15]

The anode reaction: $$M \rightarrow M^{n+} + ne^- \tag{5}$$

The cathode reaction: $$2xM^{n+} + 2nxe^- + yO_2 \rightarrow 2M_xO_y \tag{6}$$

The overall reaction: $$2xM + yO_2 \rightarrow 2M_xO_y \tag{7}$$
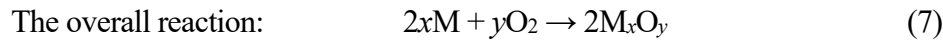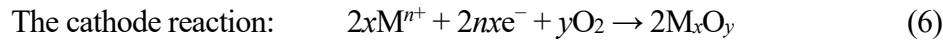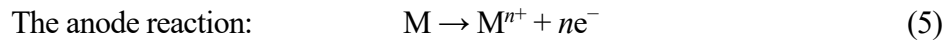
2.3 Zinc air batteries and rechargeable Zinc air batteries

Zn-air battery is a promising candidate among aqueous metal (Zn, Fe, Mg, and Al)–air batteries for the electrochemical ESS. Primary Zn-air batteries are used in hearing-aid devices for many decades due to its inherent high energy density and safety. Making the primary Zn-air battery rechargeable is attractive due to its high energy density (700-900wh/kg), low cost (currently <\$100 $kW^{-1}\ h^{-1}$, and potentially <\$10 $kW^{-1}\ h^{-1}$) , and environmentally benign. The rechargeable Zn-air battery is suitable for a grid-scale ESS. However, it was quite challenging to make the Zn-air battery rechargeable.

Zinc is one of the most abundant and accessible elements in the earth's crust, at almost five times the lithium level. Zn is also considered as a sustainable material. A small amount of Zn can

be disposed of in a landfill, and the recycling of large amounts is not difficult. In the past century, billions of Zn-air primary cells and Zn-MnO2 alkaline batteries were sold in the world market.[16][17]

A typical Zn-air battery consists of four major components: a Zn metal anode a porous air cathode, an alkaline electrolyte (30% KOH solution) and a separator. During the discharge reaction, the Zn anode is oxidized to Zn^{2+} ions, combined with hydroxide ions (OH^-) becoming solute zincate ions $Zn(OH)_4^{2-}$. After reaching supersaturation, the $Zn(OH)_4^{2-}$ anions transforms into insoluble zinc oxide (ZnO).   Instead of being oxidized electrochemically, the zinc also reacts with water to generate H_2 gas in a parallel side reaction. At the air cathode, the O_2 from the surrounding atmosphere permeates the porous cathode and gets reduced to hydroxide ions (OH^-) on the catalyst surface.   The reactions of a Zn-air cell are listed below.

Anodic reactions:

$$Zn + 4OH^- \rightarrow Zn(OH)_4^{2-} + 2e^- \quad E^0 = 1.199 \text{ V } \textit{vs. } NHE \tag{8}$$

$$Zn(OH)_4^{2-} \rightarrow ZnO + H_2O + 2OH^- \tag{9}$$

$$Zn + 2H_2O \rightarrow Zn(OH)_2 + H_2 \tag{10}$$

Cathodic reactions:

$$\tfrac{1}{2}O_2 + H_2O + 2e^- \rightarrow 2OH^- \quad E^0 = 0.401 \text{ V vs. } NHE \tag{11}$$

$$O_2 + H_2O + 2e^- \rightarrow (HO_2)^- + OH^- \quad E^0 = -0.076 \text{ V vs. } NHE \tag{12}$$
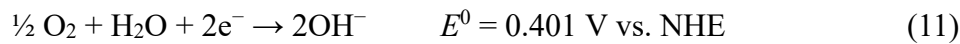
The overall reaction can be generally written as:

$$Zn + \frac{1}{2} O_2 \rightarrow ZnO \qquad E^0 = 1.667 \text{ V vs. NHE} \qquad\qquad (13)$$

In a rechargeable Zn-air battery, the reversed reactions occur during the recharging process. The ZnO is reduced to metallic zinc, which becomes deposited at the anode. However, the reduced zinc does not always settle back where it was oxidized. The non-uniform Zn deposition results in the shape change of the zinc electrode during charging. On the cathode, the hydroxide ions (OH⁻) will be catalytically oxidized and oxygen is generated at the anode.

Attempts were made to commercialize the rechargeable Zn–air batteries, e.g. , NantEnergy , EOS Energy Storage, ZincNyx.   However, the rechargeable Zn-air batteries suffer from low energy density (~35 W h kg^{-1}) [18], low power and limited cycle life compared with the state-of-the-art lithium-ion batteries. [19]

A few major barriers remain to the development of the rechargeable Zn-air batteries. One is an adequate bi-functional catalyst with the high catalytic activation of ORR and OER reactions. Pt is generally considered as the benchmark electrocatalyst for the ORR. IrO_2 and RuO_2 are for OER. However, the cost of those materials is prohibitively high for the proliferation of rechargeable Zn-air batteries.   There has been substantial research on a non-noble metal search, the highly efficient catalyst for the ORR and /or OER. The metal oxides [20, 21], the metal-free carbonaceous materials [22], M–N–C type materials [23, 24] and transition metal oxides [25] were the investigated as ORR or bi-functional catalyst. The high activity and long-term durability porous Ni-Fe nanosheets OER catalyst was reported in our phase 1 research.[26]

Another problem is the stability of the gas diffusion electrode (GDE) during recharge. Evidentially, high surface area carbon in the GDE can be oxidized during OER. The harmful side reaction substantially shortens the life of a rechargeable Zn-air battery.

Zinc irreversibility (dendrite formations, shape changes, and ZnO passivation) is another

issue that needs to be addressed. Dendrites are the uncontrolled reformation of needlelike zinc metal under specific charging conditions. A needle-like Zn dendrite can penetrate the separator and short the anode and the cathode in a rechargeable Zn-air battery. This irreversibly damages the battery. This common issue exists in the rechargeable batteries where metallic Zn or Li is used as the anode. To prevent the zinc dendrite formation, various approaches were taken. The metal ion additives, Zn metal alloys, surfactant additives or surface modification were the common method to suppress the dendrite formation. [27, 28] In a recent development, several new methods were reported, including   the construction of a high-surface-area porous structures[29], the adoption of a 3D conductive host material[30] and direct physical suppression[31]

2.4 Redox flow battery

Besides the high energy density requirement, excellent stability is another compelling character of a large scale EES.　A Redox flow battery (RFB is one of the electrochemical EES used in scale-up applications. The great scalable ability of an RFB is due to its unique battery structure- the separation of energy storage and power output. An RFB consists of three parts: the reaction unit, reactant storage tanks, and the flow system (Figure 2.2). Compared with the conventional battery structure in which the active materials are stored in the main body of the battery, a RFB has a unique feature that makes it similar to an internal combustion engine. The electrochemical reactions occur in a reactor where the active materials are pumped into the reactor and the reaction products are pumped out from the reactor. During operation, the fluids containing cathode and anode are pumped and circulated through the cathode and anode reactor, respectively. Such a configuration enables the independent control of energy and power to meet peak and base energy demand ranging from a few Kwh to several Mwh.　The total energy of an RFB system can be increased by simply adding more storage tanks.　The power can be increased by integrating more reactors when there is more electricity demand. Thus, RFBs are inherently well suited for large scale ESS in terms of efficiency over other batteries.
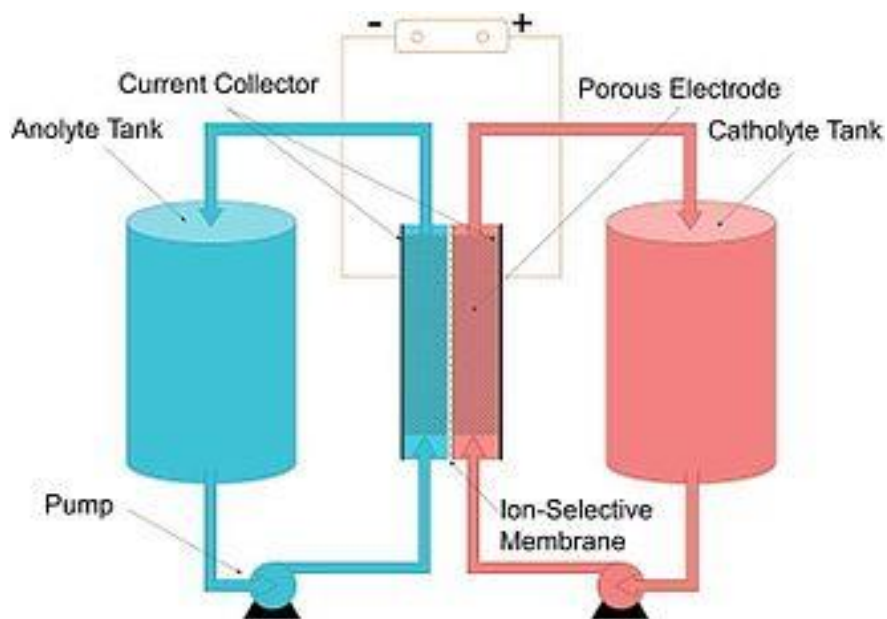
Figure 2.2 Scheme of the Redox flow battery [32]

Based on the phase of the active material, the RFBs could be divided into two major categories: all-liquid and hybrid phase batteries.[33] The all-liquid RFBs have anolyte and catholyte, in which the anode and cathode species were dissolved in the electrolyte, respectively. The all-liquid RFBs could be aqueous or non-aqueous. The aqueous system takes advantage of the adjustable pH, high conductivity and solubility. However, an aqueous RFB is limited by the water electrolysis potential windows. A non-aqueous system could be operated in a wider potential window, thus a high cell voltage. However, the high cost and complex cell engineering impede the application of the non-aqueous system. The all-liquid RFB was the first report by NASA in 1976.[34] NASA developed the first complete all-liquid RFB by using Fe(III)/Fe(II) and Cr(III)/Cr(II) redox couples, An all-Vanadium redox flow battery was invented by Skyllas Kazacos at the University of New South Wales, Australia. All-Vanadium redox flow battery was the first installed redox flow battery. It has been deployed all-round the word from KWh to the MWh scale.[35] During the past 40 years, people investigated various all-liquid redox couples, both inorganic and organic. The vanadium bromide and chloride/polyhalide RFB was reported by the Skyllas-Kazacos

research group.[36, 37] The Quinone–Bromide RFB was developed by Michael J. Aziz   research group.[38]   The benzoquinone- anthraquinone RFB was invited by   S. R. Narayanan group [39]   .Ruthenium Complexes RFB was by . Matsumura-Inoue group [40]

The hybrid phase RFBs have three subgroups in general: solid-liquid phase, gas-liquid phase, semisolid phase.   The solid-liquid RFBs have one solid species plating on the electrode. Zinc-Cerium RFB is one of the examples.   It was first proposed by Clarke and co-workers in 2004[41]. The zinc was deposited on the anode during the charging process.   The gas-liquid RFBs have a gas breath electrode , which is widely using in the metal-air battery. Yet-MingChiang group developed the Sulfur-air RFBs in 2017[42]. The semisolid phase consists of an insoluble particle suspend in the gel-like electrolyte. [43]

2.5 3D printing technology

Cell design and engineering play essential roles in developing a new EES system and improving existing technology. During the try and error process of engineering the conventional manufacturing technique (subtractive manufacturing) is expansive and limits the freeform construction. For example, the investigations of a sandwich-type electrode and the current collector's complex structure are challenging by using subtractive manufacturing.The remnants will be a big waste.

Additive manufacturing (AM) refers to building a 3D object by adding layer-upon-layer of material directly controlled by a computer aid-design (CAD) design files. It is a novel class of fabrication technologies that offer tremendous freedom to fast create a complex architecture at a lower cost than conventional subtractive manufacturing. [44] The technology was patented by Charles Hull in 1986 in the process known as stereolithography (SLA).   After more than 30 years of development, technology has become a widely accessible and low-cost fabrication method. Its applications can be found in many industries, including biomedical, aerospace, construction [45] Additive manufacturing has also been applied in the design and optimization of an EES, including Laser-based 3D printing, Electrodeposition-based 3D printing, Extrusion-based 3D printing [44].

Based on the energy of the laser, the laser-based 3D printing can be selective laser melting (SLM) (high energy laser beam) and selective laser sintering (SLS) (low energy laser beam). SLM employs a high energy laser beam t to melt the power raw material fully, a homogeneous and dense part can be built layer-by-layer. A helical 3D-printed metal electrode has a report by Martin Pumera 's group [46]. SLS used a low power laser raster over the power of raw material. Since the material was not fully melted but sintered together, it is used to build a component with a porous structure.

Liu et al. report to use SLS to create 3D hierarchical porous metallic scaffolds for energy storage devices. [47]

Electrodeposition-based 3D printing refers to coat the desired material on the surface of a substrate by applying an electric field.   Electrophoretic deposition (EPD) is one of the popular electrodeposition-based 3D printing methods. An EPD system consists of a power supply, a conductive substrate, and a counter electrode. When the electric field is applied, the liquid suspension's desired material particles were deposited on the substrate.[48] Hunag et al. fabricated a binder/additive free composite electrode of lithium iron phosphate/reduced graphene oxide with ultrahigh lithium iron phosphate mass ratio by EPD.[49] Yang et al. reported a binder-free silicon (Si) based electrode for lithium-ion battery which was fabricated in an organic solvent with EPD [50] In order to fine-tune the morphology and structure of the deposited film, electrodeposition on a pre-engineered template was adopted to fabricate an electrode with complex microstructure for an EES application. Wang et al. designed a novel NiP@CoAl-LDH nanotube arrays (NiP@CoAl-LDH NTAs) on Ni foam via template-assisted electrodeposition for the electrode of the supercapacitor. [51] Pikul et al. reported a three-dimensional bicontinuous interdigitated microelectrodes of lithium-ion micro-batteries [52]

Extrusion-based 3D printing employs a X-Y-Z-axis motion stage to print patterns by squeezing "ink" through a micro-nozzle. Inkjet printing and direct ink writing are the two most widely used methods for EES applications.[53]   Inkjet printing uses the droplets of ink-like active material to print a thin film or a substrate pattern.The thinness of the material can be controlled by tuning the flow of the droplets. Xu et al. formulated a graphene/polyaniline (NGP/PANI) inks and produced a NGP/PANI thin-film electrode for supercapacitors. [54] Ho et al. reported the first inkjet-printed zinc-silver 3D micro battery.[55]. Direct ink writing is based on the extrusion of a paste-like

active material on a substrate. Wei et al. demonstrated the fabrication of LIBs micro batteries by direct writing of cathode, LFP, and anode, Li4Ti5O12 (LTO), inks. [56] Fu et al. developed a graphene oxide-based electrode and solid-state electrolyte inks to achieve all-component 3D-printed lithium-ion batteries.[57]

2.6 NI LabVIEW based control and monitor system

A control and monitoring system are necessary for a large scale electrochemical EES. The data acquisition of control and monitoring systems requires high acquisition rates and precise synchronization between the control and the measurement. [58] Among the commercial solutions on the market, National Instruments (NI) LabVIEW platform is one of accessible r environment in industrial automation, testing automation, instrument control, data acquisition and monitoring systems.   It provides the flexibility to integrate the data acquisition hardware and control algorism software for automation control and monitoring applications. The platform includes the LabVIEW software and the hardware, NI Multifunction I/O Device or third parties I/O Device like Arduino or Raspberry Pi.

LabVIEW (Laboratory Virtual Instrument Engineering Workbench) is a high-level graphical programming environment. It offers users of any background the possibility of building control, monitoring, and test programs through visual programming, especially for those familiar with programming concepts but are not professional software developers but rather domain experts [59]. Scientists and engineers can create programs based on their innovative ideas.   The LabVIEW is highly modularized. The LabVIEW uses function nodes, wire, structure rather than code and brackets to implement the complex algorithm. A user could build a logic relation or operation between different function-nodes and variables by just connecting wires. (Figure 2.3). It can significantly reduce the development time and complexity compared with conventional programming like C/C++ or Java which is code-based.
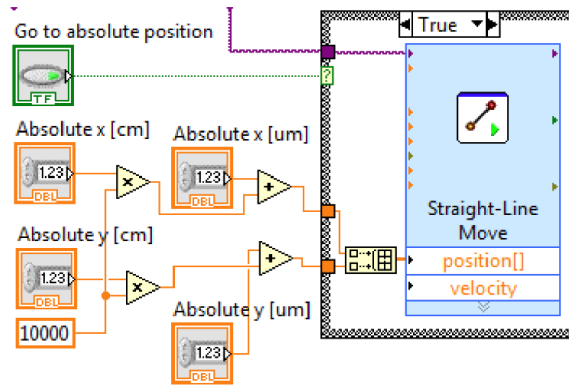
Figure 2.3 An example of the G programming language

A LabVIEW program consists of one or more virtual instruments (VIs). Virtual instrument is a concept referred to as the software-based instrument imitating an actual physical instrument. The VI has two panels to imitate the interface of a physical instrument and its circle board separately. The front panel displays the graphs, parameters and text, adjustment of the parameters, on/off switch, function selections. (Figure 2.4 A). The back panel (the block diagram) consists of the actual program of VI, which is made of built-in functions, constants, wires and structures. Every front panel component has a terminal in the block diagram (Figure 2.4 B). The front panel and block diagram cannot work independently.
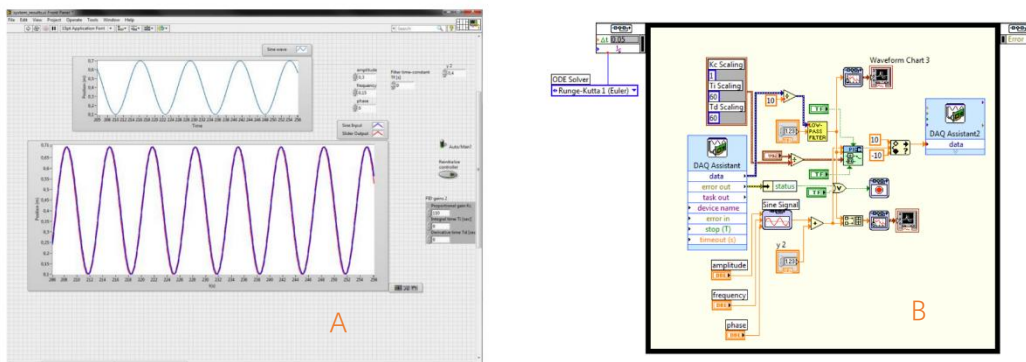
Figure 2.4 An example of the VI

LabVIEW is also a dataflow programming language, which is another distinguishing

feature. The dataflow model refers to the flow of data throughout the runtime of VI. A function node in the block diagram executes when it receives all required inputs.   It produces output data and passes the data to the next node in the dataflow path. The movement of data through the nodes determines the execution order of the VIs. In most code-based programming languages like C or JAVA, a program's execution order was determined by the sequential order of program elements (scripts), which is a control model. In LabVIEW, the flow of data rather than the sequential order of scripts determines block diagram elements' execution order. Therefore, the user can create block diagrams that have simultaneous operations. Because of the dataflow model, LabVIEW can execute multiple operations in parallel which is a benefit for a time-critical application like real-time control and monitor.

LabVIEW program can be compatible with t various hardware including NI Multifunction I/O Device and third party I/O Device like Arduino (Figure 2.5). NI developed riches of multifunction I/O device, which can communicate with VI and implement the function of VI. The multifunction I/O devices provides a combination of analog I/O, digital I/O, and counter/timer functionality in a single device for computer-based systems. It offers a mix of I/O with varying channel counts, sample rates, output rates, and other features to meet many common measurement requirements. The third party I/O device or microcontroller is also programable by LabVIEW. The Arduino was one of the popular microcontroller board. Arduino is an open-source platform based on a simple microcontroller board.   NI developed the LabVIEW interface for Arduino, which make full use of LabVIEW powerful VI library to work with Arduino.

Figure 2.5 LabVIEW compatible hardware

Chapter 3 The reactor performance improvement by cell design optimization

3.1 Introduction

We continued to optimize the reactor's design to increase the specific current density (mA per cm2) and the durability of the GDEs). The first-generation design (Gen 1) was focused on maximizing the air cathode's interfacial area and the smooth flow of the zinc slurry through the reactor during discharge. The Gen 1 design had a set of the bi-air electrode in parallel to increase the interfacial surface area. The Gen 1 design was focused on reducing the non-reacted "dead zinc" and increasing the anode current collector's surface area.

The frame of the reactor was fabricated by two different commercially available plastic-PVC and PTFE. PVC is excellent electrical insulator and has an excellent chemical resistance to strong alkaline e.g. 30- 50% potassium hydroxide. One of the drawbacks of PVC is its low thermal stability. Polytetrafluoroethylene (PTFE), also known as Teflon™, is one of the most widely used fluoroplastic material. PTFE offers excellent properties such as a high melting point (about 327°C), chemical inertness, low friction coefficient, negligible water absorption, non-adhesive, and anti-stick. It also has high electrical resistance, even in wet environments. PTFE also has some drawbacks like high density, low wear resistance, high elongation, and low resistance to compressive deformation, a challenge for machining and prototyping.

3.2 Experimental

3.2.1 Reactor cell design

3.2.1.1 The architecture of the Gen 1 reactor
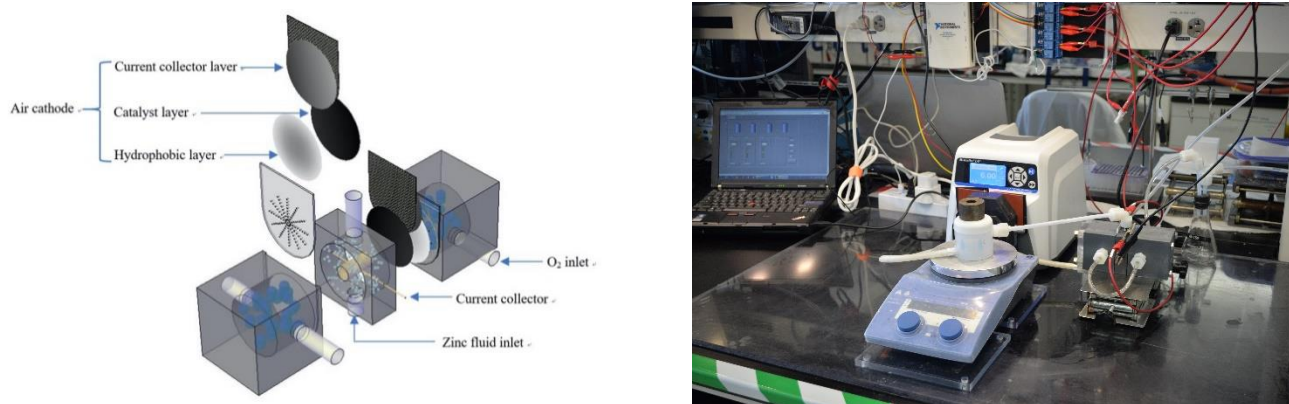
Figure 3.1 The 1st generation architecture of the reactor

The Gen 1 reactor's architecture was configured to accommodate two cathodes in parallel, as shown in Figure 3.1 The bi-electrode set-up allowed doubling the cathode reaction area. The GDE was constructed with three layers (shown in Figure 3.1 A): a catalyst layer, a current collector layer, and a hydrophobic gas diffusion layer. The geometric surface area was 5 cm^2. The catalyst layer was made from high surface area active carbon powder with manganese oxide as a catalyst and PTFE as a binder. The current collector was a carbon cloth pressed on a woven nickel mesh. The hydrophobic layer was a porous Teflon film (POREX PTFE membrane PM21M). The anode current collector was a brass rod. The separator to separator cathode and anode reactors was a non-woven separator (Celgard 5550).

3.2.1.2 The Gen 2 and Gen 2.5 reactor architecture
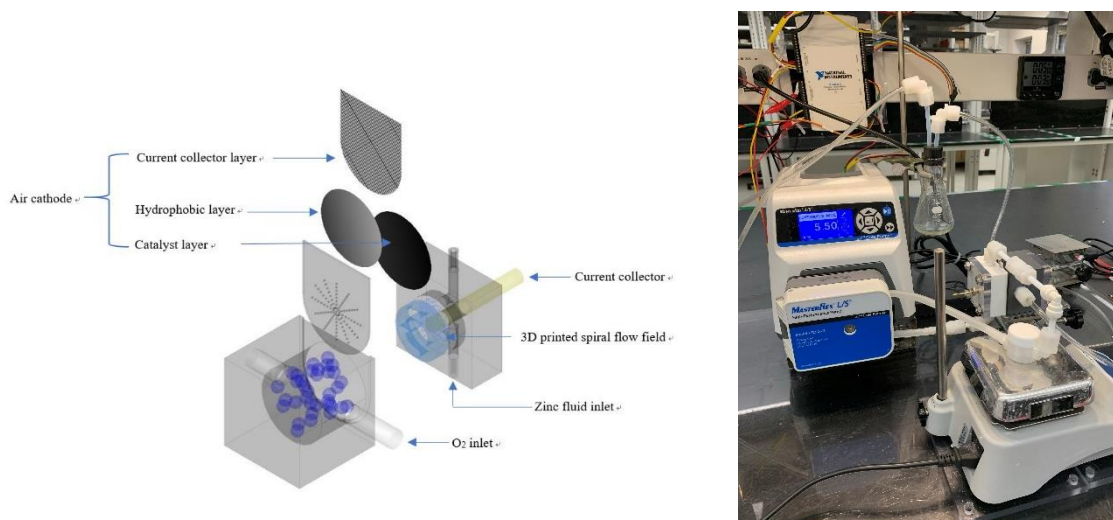
Figure 3.2 The 2nd generation architecture of the reactor

The Gen 1 reactor consisted of a single cathode, due to the low volume utilization and the accumulation of "dead Zn" in the Gen 1 design. In the Gen 2 design, an innovative 3D spiral flow field (shown in Figure 3.10) was designed and used to guide the zinc slurry flow inside the reaction chamber. The "dead zinc" was significantly reduced compared to the open flow field in the Gen 1 design.

Another important role the spiral flow field played was to support the air cathode physically. The air cathode in the Gen 1 design was suffered from the detachment of the catalyst layer with the current collector during operation. The volumetric efficiency for the Gen 2 design was substantially increased.

In the Gen 2.5 design, the plastic 3D flow field was replaced by a metal 3D flow field.   The 3D metal flow field itself is the current collector for Zn anode, so Zn slurry's contact surface and contact time were significantly increased, leading to more uniform Zn oxidation during discharge and less "dead Zn".

3.2.2 The material of cell architecture

The reactors were fabricated with both PVC and PTFE. The same air cathode, current collect, and zinc slurry composition experiment conditions were used in both reactors. The clogging event was recorded to investigate the effect of flow frame material.

3.2.3 Anode current collector design

The different current collector design was investigated. Different sharps (2D and 3D), different width, and different depth of the flow channel were studied. The current collector plays an essential role in increasing the reaction contact area and reducing the "dead zinc." Due to the Non-Newtonian fluid behavior of zinc slurry, the clog was likely to happen during cell operation. The clog causes irreversible damage to the flow system. The appropriate size of the 3D current collector would be the key to improving the system's durability.

3.2.4 The performance of the reactor

The cells with different architecture design, material, the current collector design were assembled and tested. The performance tests included multiple-step constant current discharge with a pause in between.   The plateau voltage was plotted to characteristic the performance.   In the full cell discharging performance measurements, the discharging units, including one reactor,

one peristaltic pump, one magnetic stirrer, and one zinc fluid storage tank, were employed.　The discharging tests were performed at 25 °C at constant pump speed and a constant gas flow rate.

3.2.5 The PEIS evaluation

Potentiodynamic electrochemical impedance spectroscopy (PEIS) was used to assess the cell's Ohmic resistance under static conditions. The system's overall resistance was taken as the real component of the impedance when the imaginary impedance equaled zero. The value of the true Ohmic resistance was determined from a Nyquist plot when the curve intersected the real axis. The experiments were replicated three times.

3.3 Results and discussion

3.3.1 Reactor cell design
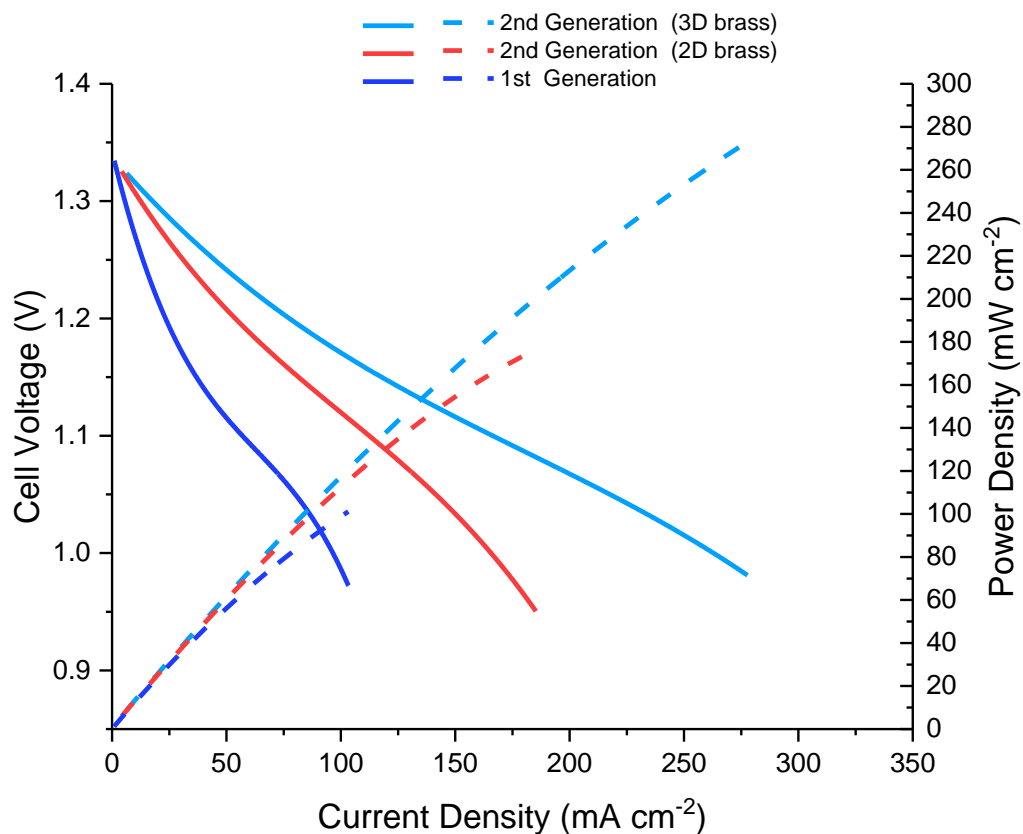
Figure 3.3 The polarization characteristics teste of cells with the different generation

The polarization curves of the reactors of different designs are shown in Figure 3.3. The Gen 2 3D reactor design improvement clearly demonstrated substantial improvement on the current density and power density. The two significant issues in the Gen 1 reactor were inefficient zinc particle utilization and the delamination of the air cathode. In the Gen 1 design, due to the volume of the anode reactor and the free flow field, not all the Zn particles gained physical contact with the current collector, so the oxidation of the Zn was not uniform. In addition, residual Zn particles may be trapped in the corner of the free flow field and became the "dead Zn". The "dead

zinc" expropriated the useful raw zinc from the slurry, which resulted in increased impedance of zinc slurry electrode and errors in the flow management based on the charge transfer balance of the depth-of-discharge (DoD). The air cathode suffered from delamination during the operation due to the lack of support at the side of the zinc slurry. In order to address both issues, a 3D-spiral flow field was introduced in the Gen 2 design. The flow field guided the zinc slurry through the react. The guided flow ensured all the zinc particles passing through the reactor sequentially, and no residual or "dead Zn" remained. The solid flow field can provide hard support for the air cathode to mitigate the delamination.

The engineering challenge was that Zn slurry clogging was more likely to occur in the track of the flow field. Indeed, Gen 2 reactor was more likely to be clogged than that of Gen 1. The problem of clogging remains to be solved. The anode current collector in the Gen 2 reactor was changed to a flat metal disk next to the spiral flow field plate. The anode current collector in the Gen 1 reactor was a brass rod. Apparently, the contact area of Zn slurry with the current collector was significantly increased.

In the newest Gen 2.5 reactor design, an integrated spiral flow field made by metal 3D printing was used as a flow field and current collector. With the Gen 2.5 design, the contact area of Zn slurry and current collector was maximized, which further improved the performance of the reactor. The power density was up to 280 mW cm^{-2}, and the current density was up to 280 mA cm^{-2} (Figure 3.3) at a constant flowing rate (at 0.95V cut off voltage), which was almost 3 times larger than that of Gen 1 design.

The PEIS test results show that the average impedance of Gen 2.5 was 30% less than Gen 2 design (Figure 3.4).,
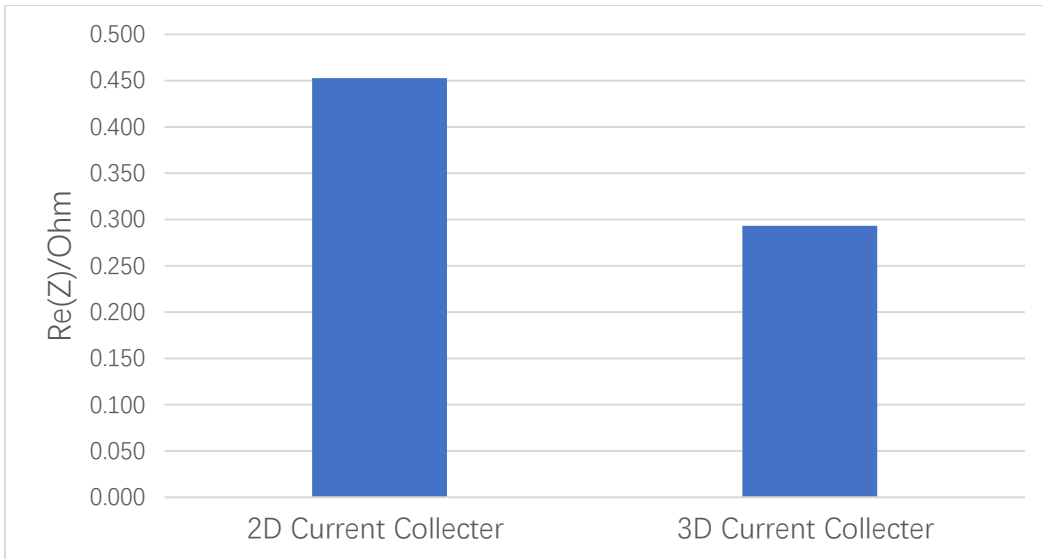
Figure 3.4 Average impedance of cells with the different current collector

3.3.2 Effect of the material of cell architecture
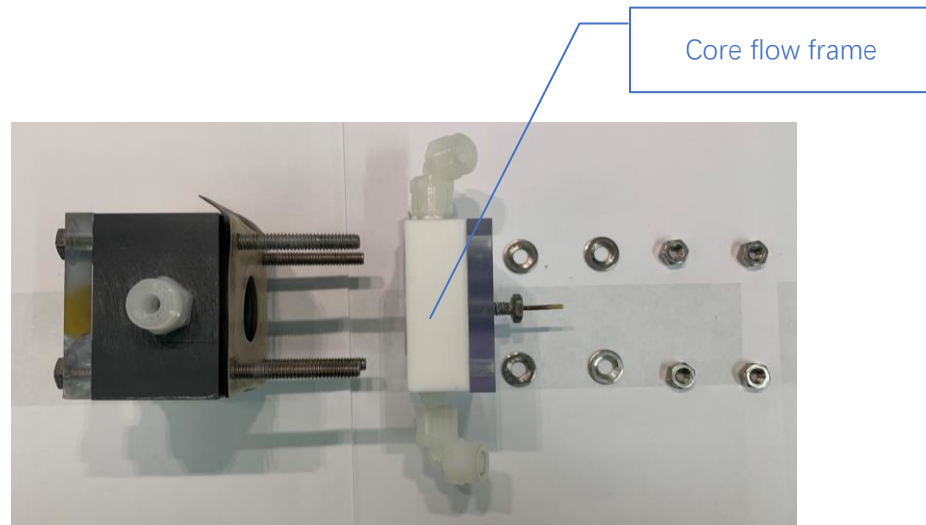
Core flow frame

Figure 3.5 Exploded view of Gen 2 reactor

Figure 3.5 shows the reactor. The core flow frame was the main body, where the electrochemical reactions occur. It also provided the space to accommodate key components like cathode assembly, separate, and anode current collector. In this experiment, the core flow frame was fabricated with two different commercially available plastics – PVC and PTFE. The polarization curves shown in Figure 3.6 shows that the PTFE core flow frame demonstrated better performance in current density and power density than that of PVC. The tests were replicated three times.
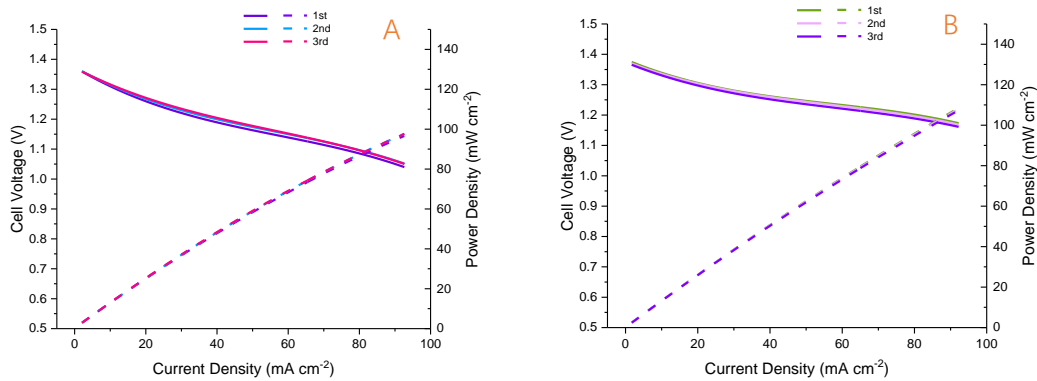
Figure 3.6 The polarization characteristics teste of cells build by PVC(A) and PTFE(B)

Polymers [1]		E (GPa)		
Elastomer	Butyl Rubber	0.001	-	0.002
	EVA	0.01	-	0.04
	Isoprene (IR)	0.0014	-	0.004
	Natural Rubber (NR)	0.0015	-	0.0025
	Neoprene (CR)	0.0007	-	0.002
	Polyurethane Elastomers (elPU)	0.002	-	0.003
	Silicone Elastomers	0.005	-	0.02
Thermoplastic	ABS	1.1	-	2.9
	Cellulose Polymers (CA)	1.6	-	2
	Ionomer (I)	0.2	-	0.424
	Nylons (PA)	2.62	-	3.2
	Polycarbonate (PC)	2	-	2.44
	PEEK	3.5	-	4.2
	Polyethylene (PE)	0.621	-	0.896
	PET	2.76	-	4.14
	Acrylic (PMMA)	2.24	-	3.8
	Acetal (POM)	2.5	-	5
	Polypropylene (PP)	0.896	-	1.55
	Polystyrene (PS)	2.28	-	3.34
	Polyurethane Thermoplastics (tpPU)	1.31	-	2.07
	PVC	2.14	-	4.14
	Teflon (PTFE)	0.4	-	0.552
Thermoset	Epoxies	2.35	-	3.075
	Phenolics	2.76	-	4.83
	Polyester	2.07	-	4.41

Table 3-1 Young's modulus of Plastics [60]

According to table 3-1, PVC has 5-8 times higher Young's modulus than that of PTFE. That means a PTFE would be much more compressible than PVC. The PTFE core flow frame would transfer more stress to the cathode assembly (Figure 3.2) than the PVC core flow frame, which reinforces the connection between the catalyst layer and the current collector of the cathode. The better connection would reduce the full cells' impedance, confirmed by PEIS test results shown in Figure 3.7. The compressible PTFE core flow frame also provided a better sealing. This feature

significantly diminished the electrolyte creepage, which was observed in long term tests.
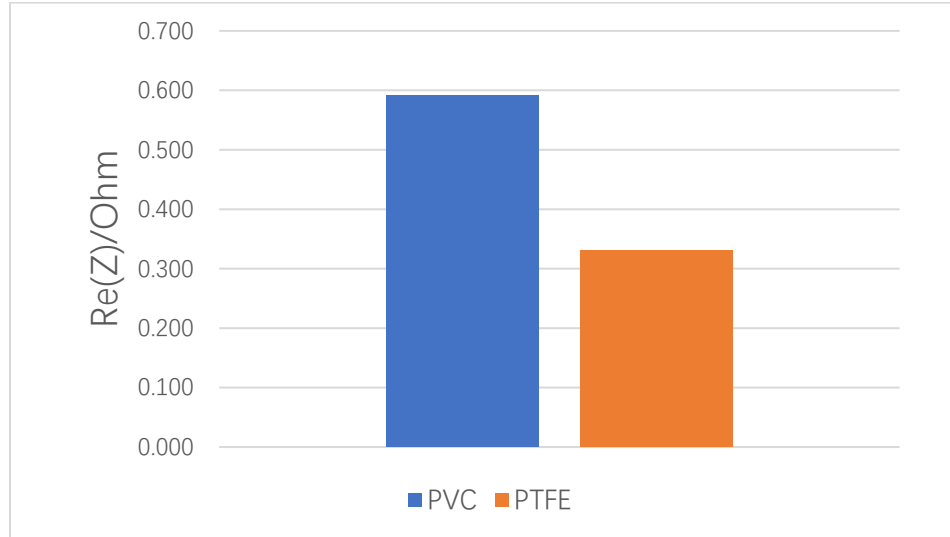
Figure 3.7 Average impedance of full cells with different materials

The clogging inside of the reactor was an issue in the Gen 2 design. The root cause of clogging was still under investigation. The clogging occurred randomly during a discharge and a standby. The clogging frequency was calculated by the numbers of clogging the event / all recorded tests. The results showed that the clogging occurred three times less in a PTFE body than that of a PVC body. Since the inlet and outlet pathways of zinc slurry were through the core flow frame, the friction could be one factor of clogging. PTFE's friction coefficient is about 0.05 to 0.10, which is the third-lowest of any known solid material (Figure 3.9).   The PVC has 3-4 times higher friction coefficient than PTFE. It is critical for the durability of the Zn-air flow cell to solve the clogging issue. The DoD, particle size of zinc electrode, gel agent, and slurry mixture procedure all contribute to the slurry electrode's flow behavior. To solve the clogging issue completely, those factors should be investigated in the next phase of research.
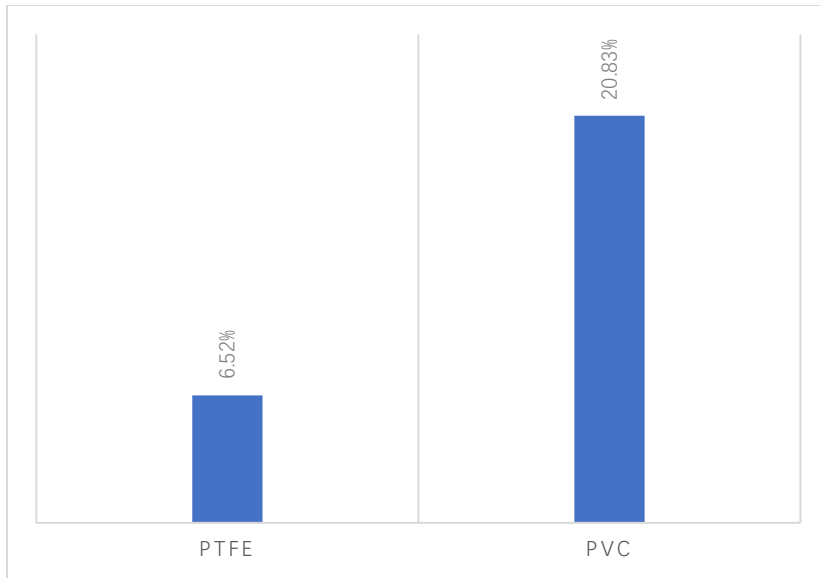
Figure 3.8 Clogging frequency of different materials
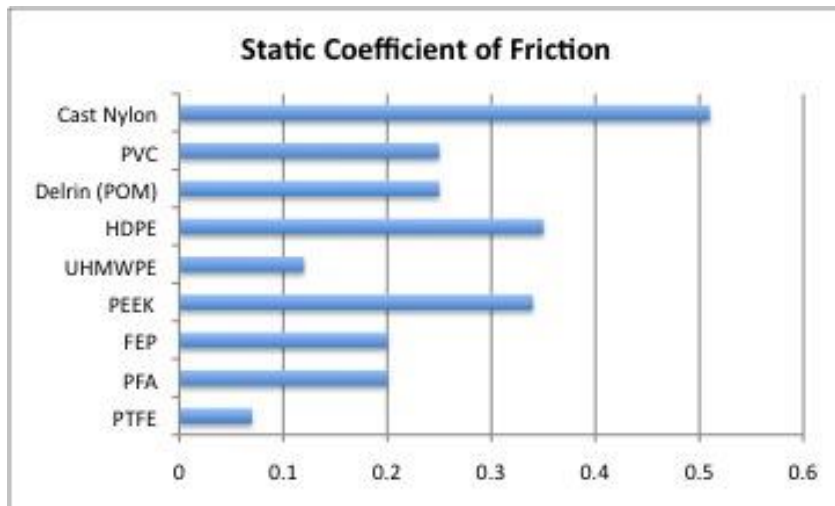
Figure 3.9 Static coefficient of friction of Plastics [61]

3.3.3 Effect of anode current collector and flow field design

The Gen 2 reactor design boosted the reactor's performance and the problems of Zn utilization and air cathode delamination were solved. The Gen 2 generation reactor used a plastic 3D printed flow field (Figure 3.10 A) and 2D disk metal current collector. The zinc particles could contact the metal disk current collector throughout the journey of flow in the flow field instead of the partial contact with the brass rod current collector in Gen 1 design. The Gen 2.5 reactor continued to improve contact by using metal 3D printing technology to integrate the current collector and flow field together (Figure 3.10 B&C). The metal 3D printed anode current collector was fabricated in different sharps to investigate the performance's impact.
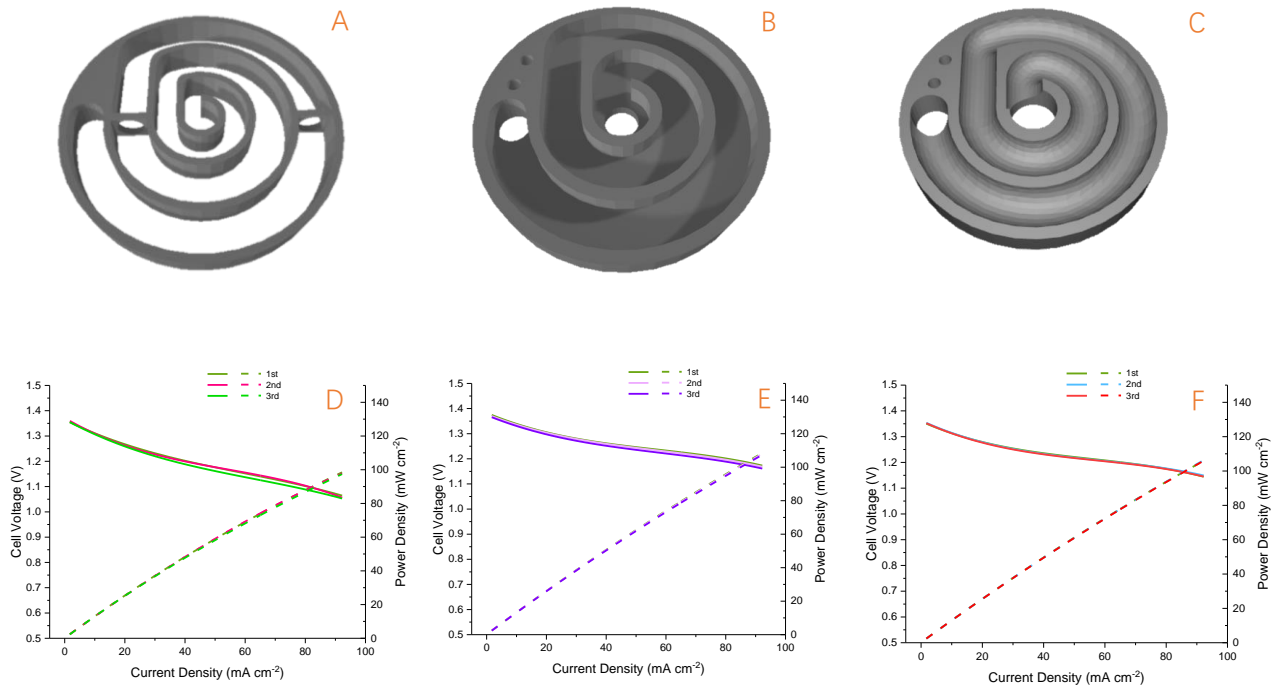
Figure 3.10　The polarization characteristics teste of cells with different anode current collector and flow field design

Better performance was demonstrated in the Gen 2.5 reactor than that of Gen 2 design. Slightly difference can be seen for the two Gen 2.5 flow field patterns (Figure 3.10 E&F).

The whole metal body of the Gen 2.5 flow field itself was a current collector that provides 3D contact to the Zn particles flowing the flow field tracks. In the Gen 2 design, since the flow field was made with plastic, the Zn only had one-dimension contact with the metal plate on the bottom.

3.4 Conclusion

The reactor is one of the critical components of the zinc-air battery system. It is responsible for generating the electricity from the electrochemical reaction between the zinc and oxygen. Thus, it is the highest priority of this project to optimize the reactor design in this project.

The engineering design of the reactor evolved twice, and the performance was tripled. That enhancement was benefited from the development of additive manufacturing processes (3D print). It provided much more freedom of design to fulfill requirements than that of conventional subtractive manufacturing. The 3D printed flow field guided the zinc slurry flow through the reactor. The efficiency of Zn reaction and the stability of Zn slurry's flow behavior were improved than that in the free flow field in Gen 1 design. The 3D printed flow field also reinforced the air cathode structure and slowed down the impedance growth, which would improve the reactor's performance and durability. The metal 3D printed flow field - current collector in Gen 2.5 design better facilitated charge transfer and mass transfer in the electrochemical reaction.

The material of the core flow frame and the design of the anode current collector were investigated to reduce clogging and improve system performance. PTFE shown superiority in terms of reducing the impedance and clogging over PVC. The Gen 2.5 outperformed the Gen 2 by

providing another dimension of contact between the current collector's zinc particle and surface.

The root cause of clogging and the discrepancy between the flow field's various shapes - current collector complex still needed more research to study in the next phase research.

Chapter 4 Air cathode fabrication and

optimization

4.1 Introduction

In general, the air cathode was the performance-limiting factor of an aqueous metal-air battery. It is also the most expensive battery component if a noble metal catalyst is used. During discharge, the ORR occurs on the air cathode. The O_2 from the ambient atmosphere passes through the porous gas diffusion layer and becomes reduced to hydroxide ions (OH^-) on the catalyst layer.

An air cathode consists of three major components: a current collector, a gas diffusion layer, and a catalyst layer (Figure 1). The current collector is usually a conductive metal mesh or foam, such as nickel and stainless steel. The gas diffusion layer (GDL) allows the permeation of O_2 gas and provides the abundant gas-liquid-solid three-phase interface for ORR. The GDL should keep hydrophobic to prevent it from the flooding of electrolytes. The catalyst layer is where the ORR takes place, so it should be kept hydrophilic to allow the electrolyte to go through the microchannels to meet the O_2 molecules at the three-phase boundary. The catalyst layer was fabricated by mixing a catalyst, a carbon material, and a binder. In most cases, the catalyst layer is pressed on the current collector and in contact with the electrolyte, while the GDL faces the open air. The current collector is placed in the middle of the catalyst layer and gas diffusion layer, forming a sandwich structure [62]. (Figure 4.1)
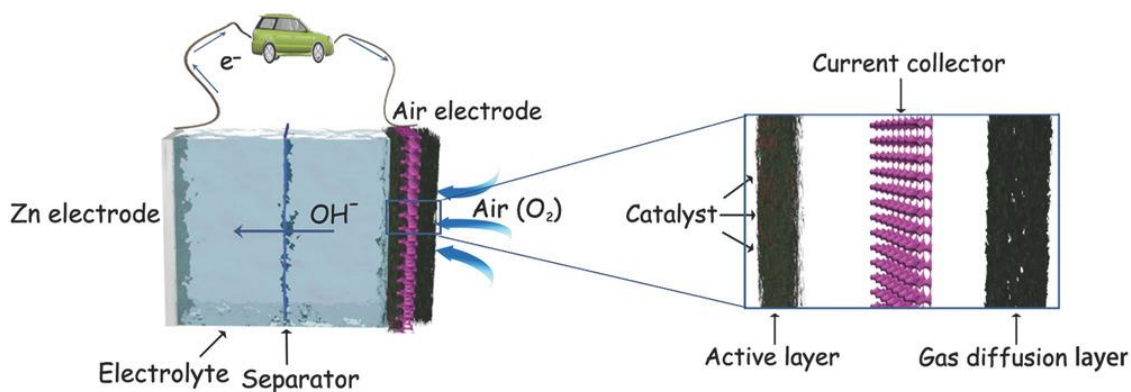
Figure 4.1 Schematic illustration of Zn–air battery and air electrode.[62]

In this chapter, the study of air cathode fabrication and optimization will be discussed, the thickness, binder content, and expanded graphite content of the catalyst layer in air cathode were investigated. These parameters were believed to affect the polarization of the air cathode and full cell performance.

4.2 Experimental

4.2.1 Materials

The air cathode material includes MnO_2 catalyst-loaded acid-washed powdered activated carbon (PWA) from Calgon carbon [63], expanded graphite. A polytetrafluoroethylene (PTFE) dispersion (60wt% PTFE condensed liquid, T-30, DuPont) was used as a binder. A 3:1 isopropyl alcohol (IPA) solution was as a dispersant. The current collector was a Ni mesh (4 Ni 7-100AN) from Dexmet and a carbon cloth (W1S1009) from CeTech. The gas diffusion layer was a Porex PM21M PTFE membrane.

4.2.2 Fabrication of catalyst layer

The catalyst layer was made by mixing MnO2 catalyst-loaded activated carbon, expansion graphite, and PTFE binder. The MnO2 catalyst-loaded activated carbon and expansion graphite were mixture by ultrasonic mixer (LabRAM) with 50% intensity for 30 mins. The PTFE binder suspension and IPA solution were adding to the powder mixture. The powder mixture was stirred by a spatula to form a dough-like paste. The paste was placed in a 30C oven for 1h to evaporate the excessive water. Then paste was transferred to a preheat roll press to roll into the desired thickness. The finished catalyst layer was dried in an oven at 80 C overnight and stored in a plastic bag for future use. The parameters for improving the cathode performance were the PTFE and expansion graphite contents of the catalyst layer and the catalyst layer's final thickness.

4.2.3 Fabrication of membrane electrode assembly (MEA)

A MEA consists of a catalyst layer, a pre-trimmed woven Ni mesh, a carbon cloth, and a PTFE membrane. The catalyst layer and carbon cloth were punched to the right size. The circular thin-film catalyst layer and smooth face of carbon cloth were sandwiched with a nickel mesh in between. The sandwich structure was then laminated together by a hot pressor with 1.5 tons of force for roughly 15 seconds. The MEA was then finished by pressing a PTFE membrane on the carbon clothe with 3.5 tons of force for 3 minutes.

4.2.4 Performance and conductivity evaluation of the air–electrodes

The electrochemical performance of the Zn air flow cell reactor was evaluated using a

potential/galvanostat (MPG220, Biologic Inc.). The Gen 2.5 reactor was used as a test vehicle. The composition of the Zn slurry was 244g/200ml (30wt%) KOH + 3.6g C940 gelling agent. The pump was set at 0.5 ml/ min flowing rate.   The oxygen flowing rate was 0.1 L/min.   The polarization tests included a multiple-step constant current discharge with a pause in between.   Then the plateau voltage was plotted against current density. Electrochemical impedance spectroscopy (EIS) was used to measure the electronic conductivity of the material. The material's overall resistance was taken as the real component of the impedance when the imaginary impedance equaled zero.

4.3 Results and discussion

4.3.1 Effect of thickness of the catalyst layer
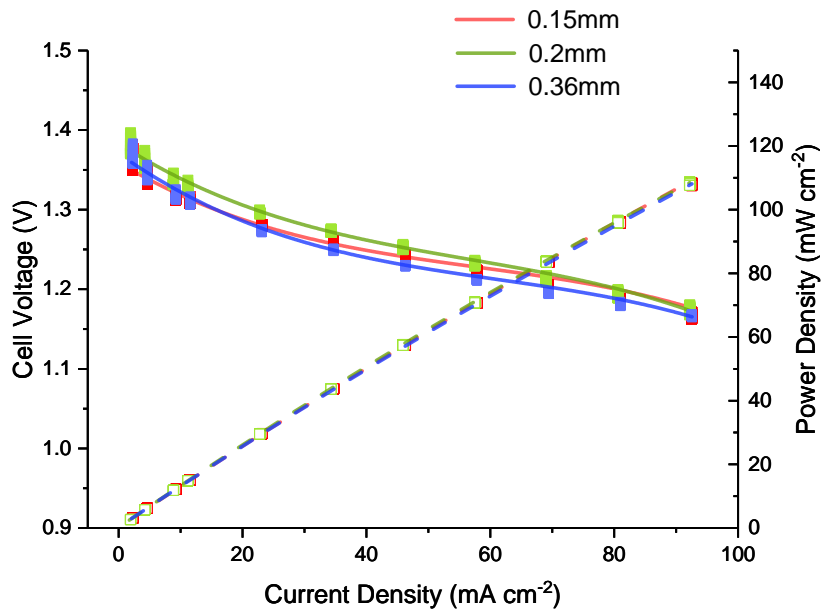
Figure 4.2 The polarization characteristics teste of cells with various thickness of the catalyst layer in air cathode

Figure 4.2 shows the polarization curves of the cathodes of 0.15,0.2 and 0.36   mm in thickness.   The cathode's PTFE content was 5 wt.%, and the expansion graphite content was 10 wt.%. The polarization curves show that the performances of the MEAs of those three thicknesses are very closed.   The conductivity is proportional to the thickness of the catalyst layer.   A similar IR drop means the conductivity was not the dominant factor of the overall performance with thickness below 0. 36mm.   A thin cathode has weak mechanical strength, which increases the opportunity of the MEA failure.   At the same time, a thick cathode uses more raw material.   The thickness of the catalyst layer of the cathode was fixed at 0.2 mm.

4.3.2 Effect of PTFE content in the catalyst layer
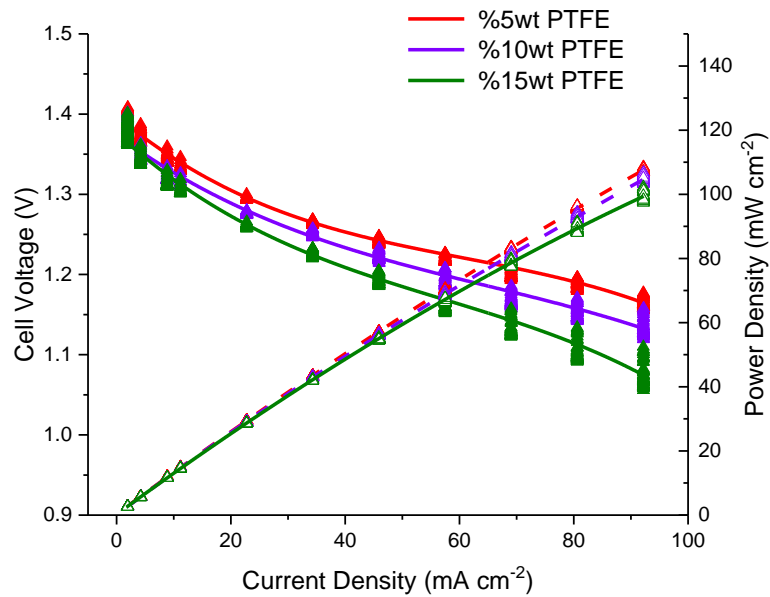
Figure 4.3 The polarization characteristics teste of cells with various PTFE content of catalyst layer in air cathode

The catalyst layer should remain hydrophilic and highly conductive. This was achieved by the optimization of the PTFE content. The catalyst layers with the PTFE content of 2.5-20 wt.% were fabricated, and their electrochemical performance was evaluated.   The expanded graphite content

was 10 wt.%, and the thickness was about 0.36 mm.   Figure 4.3 shows the polarization curves of

the catalyst layers with 5-15wt.% PTFE in the full cell. Apparently, the IR drop increased with the

increase of PTFE content. Figure 4.4 shows the electronic conductivity determined by AC

impedance.   The values were obtained by measuring and averaging three samples from different

locations of the catalyst layer sheet.   The IR drop increased with the increase of the PTFE content

since the PTFE is nonconductive. The increase of the PTFE content also a decreased the porosity

of the catalyst layer. The low porosity resulted in the decrease of the active interfacial area of

catalyst layer. The high PTFE had negative impacts on the air cathode performance because it

made the catalyst layer less conductive and less accessible. However, the insignificant PTFE

content made the MEA processing difficult for the catalyst layer. Thus, it is promising to search

for an alternative binding material with better conductivity and less impact on porosity.
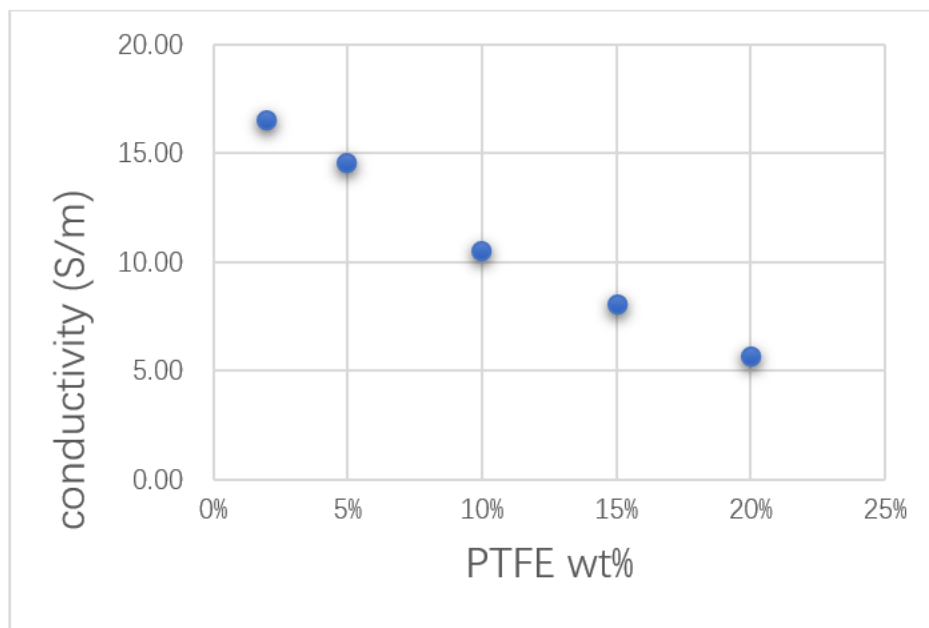
Figure 4.4 Electronic conductivity of various PTFE content of the catalyst layer

4.3.3 Effect of expanded graphite content of the catalyst layer
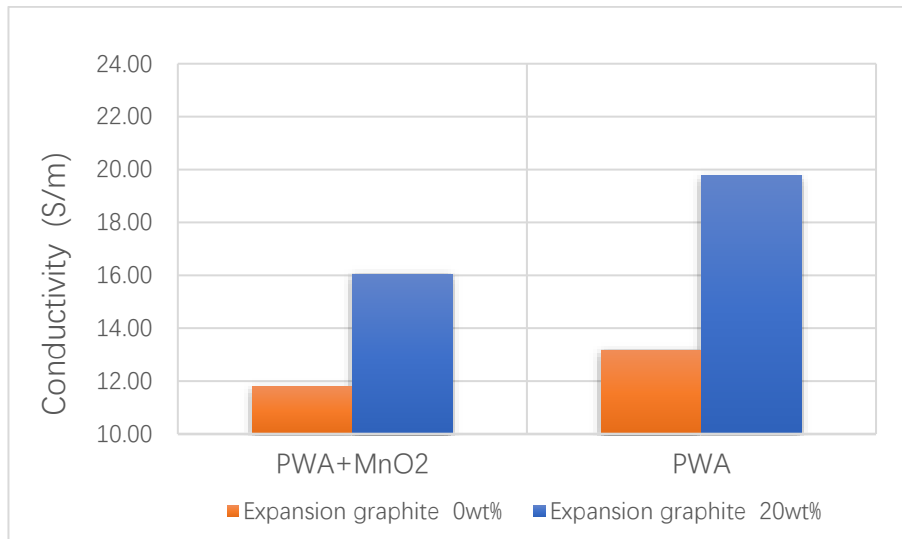
Figure 4.5 Electronic conductivity of two different expansion graphite content and MnO2 loading of the catalyst layer
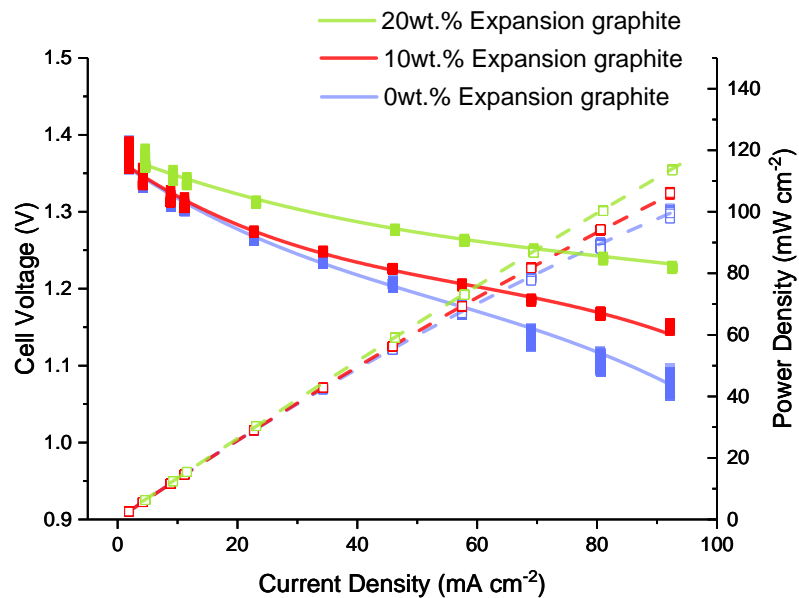
Figure 4.6 The polarization characteristics teste of cells with various expansion graphite content of the catalyst layer in air cathode

In order to improve electronic conductivities of the catalyst loaded (MnO_2 catalyst, catalyst layer, an expanded Graphite was employed to enhance the electrical conductivity. Figure 5 demonstrates that the conductivity of the catalyst layer decreases when the less conductive g the MnO_2 catalyst ($\approx 10^{-8}$ S·cm^{-1}) [64, 65] is loaded on PWA. The loss of conductivity can be mostly compensated with the addition of the expanded graphite. Expanded Graphite is made by the thermal expansion of anion intercalated. Expanded Graphite has been used in quite a few battery systems to increase the conductivity.[66] The catalyst layers with 0% 10% and 20% expanded graphite were fabricated, and their electrochemical properties were evaluated. Figure 4.6 shows the polarization curves of the catalyst layer with 0%, 10%, and 20wt.% expanded graphite in the full cell. The IR drop decreased with the increase of expanded graphite content. Figure 4.7 shows the conductivity of the catalyst layer determined AC impedance. The IR drop decreased with the increase of expanded graphite content. However, the excessive expanded graphite had a negative impact on the fabrication process for the catalyst layer. The catalyst layer with high expanded graphite lost some flexibility, which made the MEA production more difficult. The increase of the PTFE content can make air cathode more durable and flexible but less conductive; While the increase of expanded graphite can make air cathode more conductive, more porosity but less formable. Therefore, the contents of the PTFE and the expanded graphite are to be balanced and optimized. Taking into the consideration of the overall manufacturing process and the cathode's electrochemical properties, the optimum PTFE content was 5%, and expanded graphite content was determined to be 10% for zinc-air flow battery.
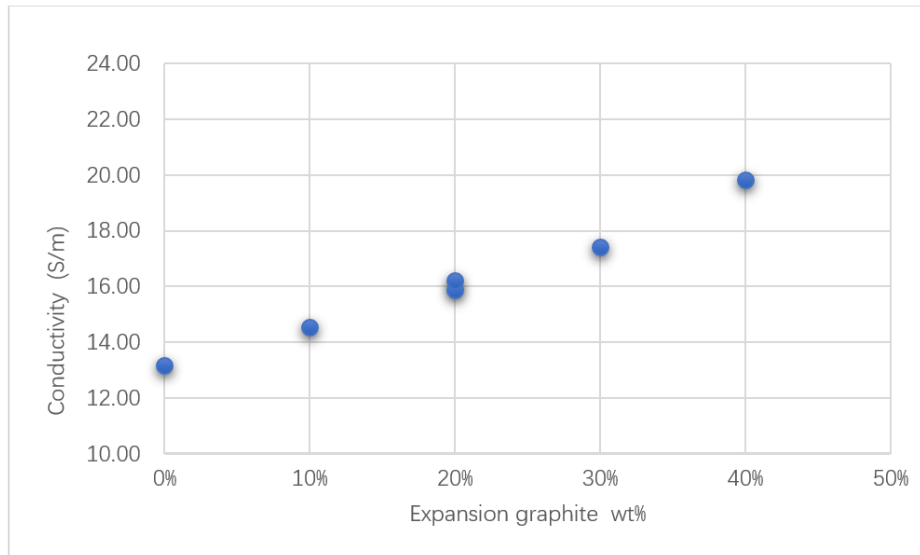
Figure 4.7 Electronic conductivity of various expansion graphite content of the catalyst layer

4.4 Conclusion

Both cathode and anode were optimized by taking into consideration of multiple engineering parameters. Poor anode performance was the bottleneck in the Gen1 reactor. With the anode improvement made in the Gen 2 reactor, the kinetics of the anode reaction was boosted. The air cathode became the limiting factor.

Three of the air cathode fabrication parameters were investigated. The optimal design of the catalyst layer with MnO_2 catalyst was determined to be:

1. The thickness of the catalyst layer of the cathode was at 0.2 mm,

2. The PTFE content was 5%

3. The expanded graphite content was 10%.

Chapter 5 LabVIEW based battery manager system building and optimization

5.1 Introduction

To ensure the smooth and safe operation of a battery, an effective battery management system (BMS) is essential. A good BMS could alleviate minor malfunction of cells in the system and prevent the battery from catastrophic failures. The Tesla Model 3 (best-selling EV) used 2170 Lithium-ion cells. The advanced BMS system of tesla counterbalances the cost vs performance and enable Tesla to meet both the price and performance targets.

The zinc-air flow battery system is designed to reduce every Zn particle to a certain depth of discharge (DoD). The principal needs to be coded in the BMS, so the DoD of Zn remains constant at any conditions of discharge power.

In this chapter, a National Instruments LabVIEW based BMS is discussed. LabVIEW platform is an accessible environment in industrial automation, testing automation, instrument control, data acquisition, and monitoring systems. It is high flexible for the integration of and data acquisition hardware and a control algorism software to automation control and monitor applications. The platform includes the LabVIEW software and the hardware, which could be NI Multifunction I/O device.

5.2 Experimental

5.2.1 System schematic
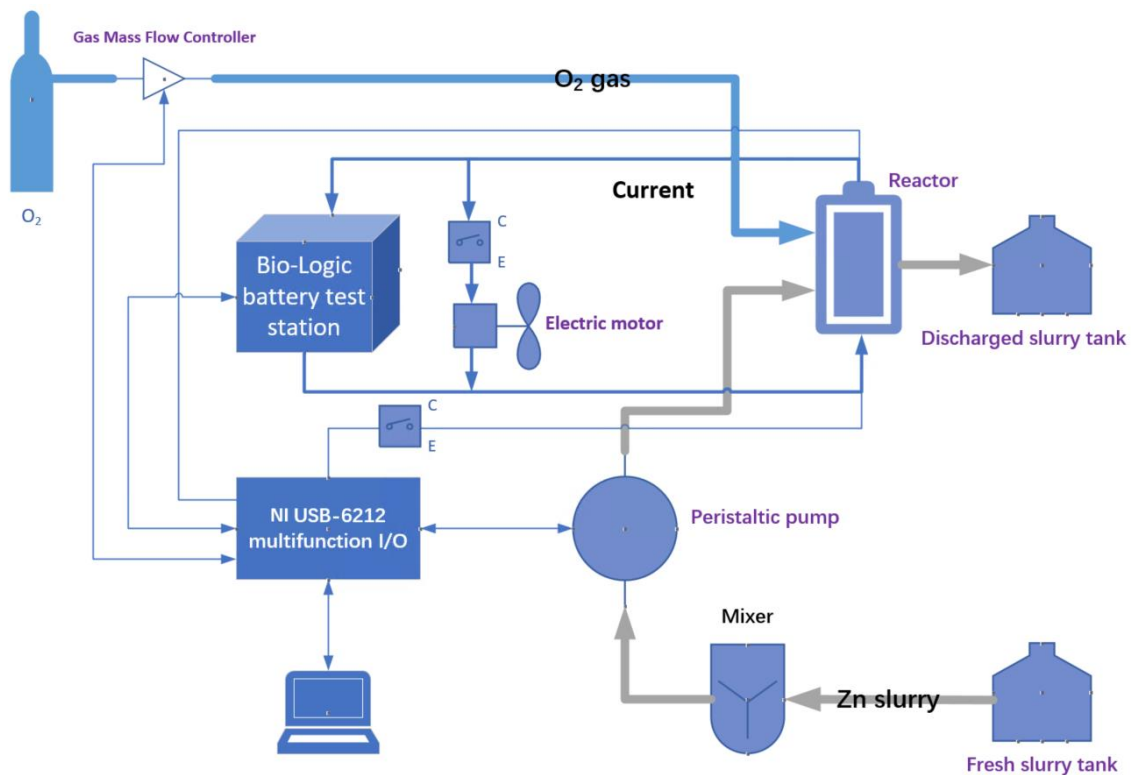
Figure 5.1 Control system schematic

5.2.2 Hardware

5.2.2.1 NI USB-6212 Multifunction I/O Device

The NI USB-6212 multifunction I/O device offers 16 analog inputs (16-Bit Analog-to-Digital resolution, sample rate 400 kS/s, 50ns Timing resolution), 2 analog outputs (16-Bit Digital-to-Analog resolution, update rate 250 kS/s, 50ns Timing resolution), up to 32 digital inputs/outputs,

and two 32-bit counters. (Figure 5.2 & Figure 5.3). It communicates with PC via a USB 2.0 cable,

which provides excellent compatibility for any laptop and desktop. The max range of analog Input

is -10V t0 10V, which indicates the 305 uV resolution. The analog output range is -10V to 10v as

well

Figure 5.2 NI USB-6212 multifunction I/O
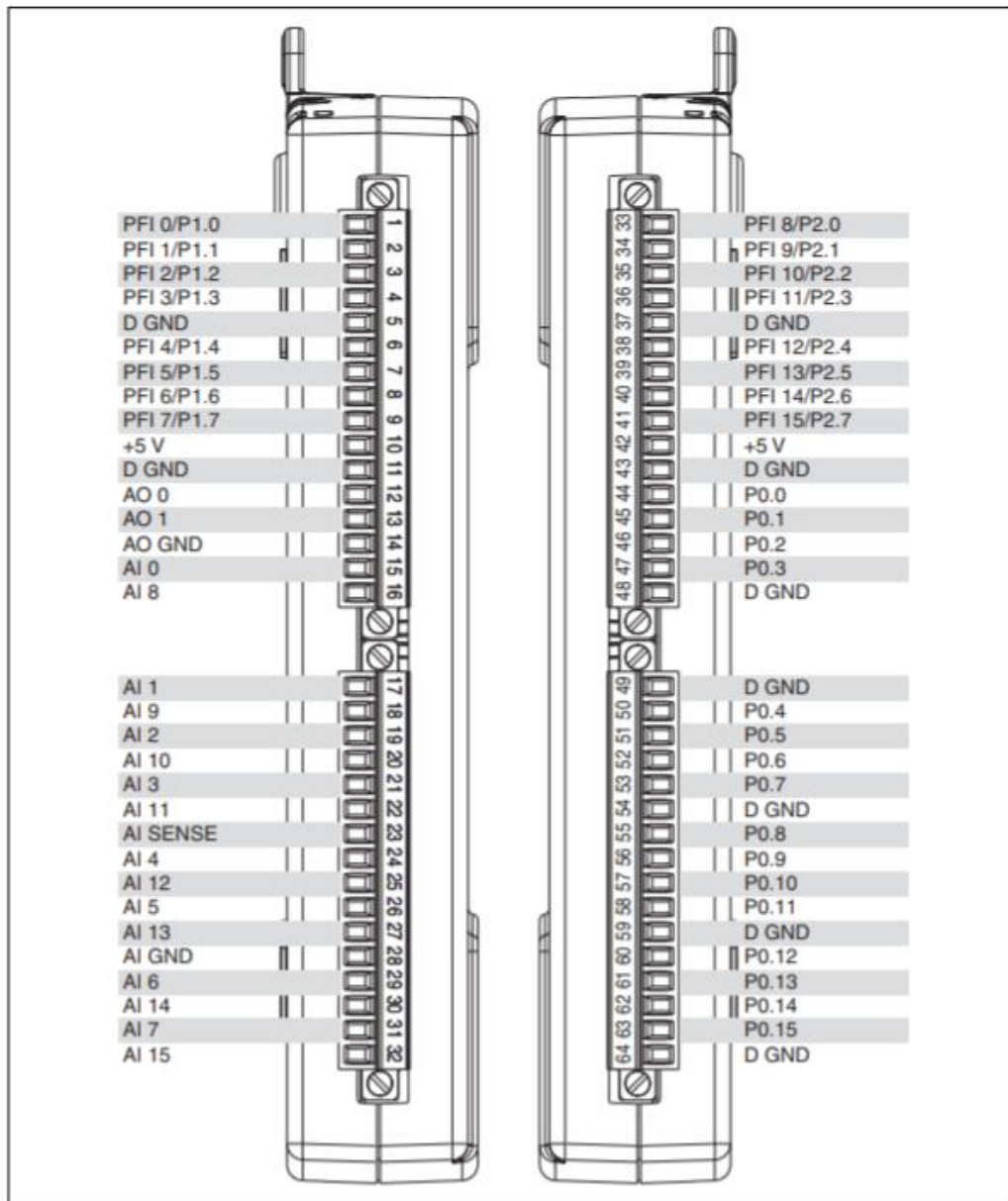
Figure 5.3 USB-6212/6216 Screw Terminal Pinout[67]

The I/O Device requires NI-DAQmx driver software (vision 17.6 for LabVIEW 2014) pre-install. Once install the NI-DAQmx driver and connect the I/O device with pc, the device will be detected by PC (Figure 5.4). "Test this device" option could validate the device function without any LabVIEW VI.   (Figure 5.5). It provides an option to acquire and generate signals to test the communication with the system's sensor and controllable component.

In the project, 4 analog inputs, 2 analog outputs, 2 digital inputs/outputs were used for pump, gas flow meter, voltage sensor, bio-logic input/output.

Figure 5.4 The window of hardware detection
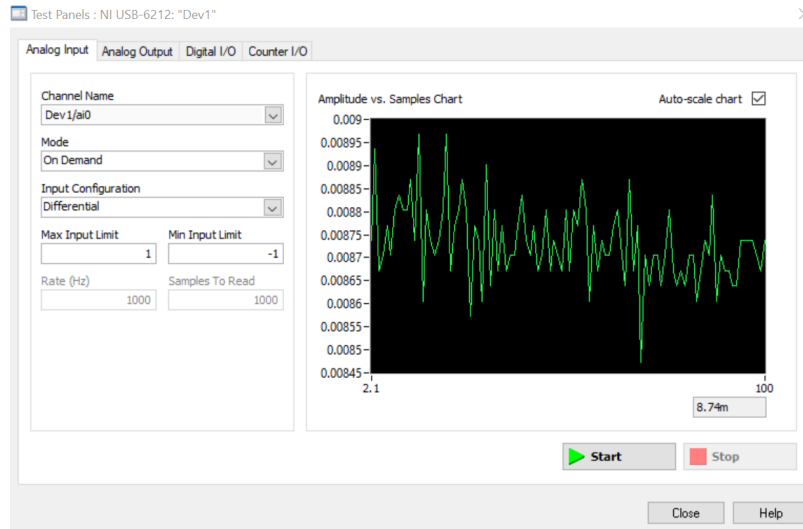
Figure 5.5 The window of hardware test

5.2.2.2 Controllable peristaltic pump

The pump used in the project was Masterflex L/S Digital Drive, 100 RPM with Masterflex®
L/S® High-Performance Pump Head. The tubing was Masterflex L/S® Precision Pump Tubing,
C-Flex® ULTRA, L/S 25.

Figure 5.6 Masterflex L/S® Digital Drive

The remote-control interface (DB-25) of the digital drive was connected to a NI USB-6212
Multifunction I/O Device. The speed control voltage input (port 1) (Figure 5.6) was connected to
the analog output (port 0) (Figure 5.3) of the NI USB-6212, and the Speed Control Input Ground
Return (port 3) was connected the analog output GND (port 14) of NI USB-6212. This couple of
connections were for the signal of speed control according to the demand. The Remote Start/Stop
Input (port 15) and remote Start/Stop, CW/CCW, Prime Grand Ref. (port 17) were connected to
the port 47 and the port 48 of NI USB-6212 separately. This couple of connections were for the
signal of start/stop according to the system status.

A. START/STOP
B. CW/CCW
C. OUTPUT 0-20mA; 4-20mA
D. INPUT 0-20mA; 4-20mA
E. INPUT 0-10V
F. OUTPUT 0-10V
G. TACH OUTPUT

H. PRIME
I. MOTOR RUNNING N.O. C(1A @ 24 V)
J. MOTOR RUNNING N.C. (1A @ 24 V)
K. 24V (150mA max.)
L. General Alarm
M. Local.Remote Indicator
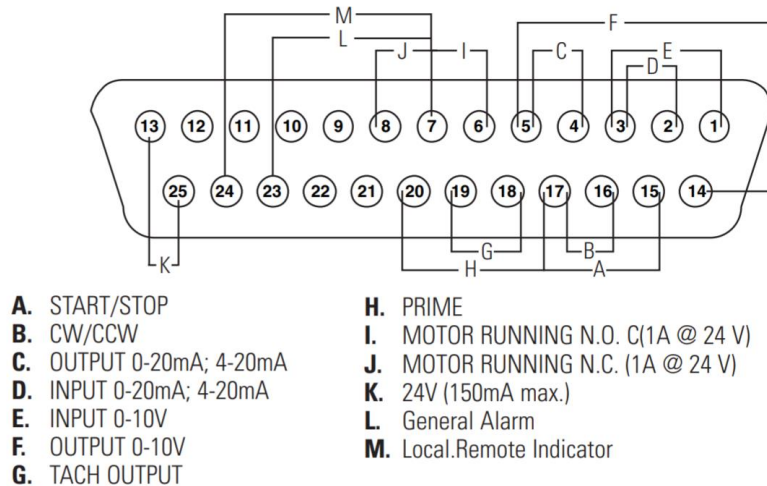
Figure 5.7　DB-25 Pin Configuration with Wiring Scheme of Masterflex L/S® Digital Drive [68]

Pin No. DB-25	Description
1	Speed Control Voltage Input (0-10 V)
2	Speed Control Current Input (0-20 mA)
3	Speed Control Input Ground Return
4	Speed Signal Current Output (0-20 mA)
5	Speed Signal Output Ground Reference
6	(Motor Running N.O. Default) 1A @24 V (Open Collector)
7	Motor Running Ground Return
8	(Motor Running N.C. Default) 1A @24 V (Open Collector)
14	Speed Signal Voltage Output (0-10 V)
15	Remote Start/Stop **Input**
16	Remote CW/CCW Input
17	Remote Start/Stop, CW/CCW, Prime Grnd Ref.
18	Tach Ground Reference
19	Tach Output (open collector)
20	Remote Prime Input
9	Reserved – Not Used
10	Reserved – Not Used
11	Auxiliary Input (Computer Compatible Drive Only)
12	Auxiliary Input Return (Computer Compatible Drive Only)
21	Auxiliary Output #1 (Computer Compatible Drive Only)
22	Auxiliary Output #2 (Computer Compatible Drive Only)
23	General Alarm (Open Collector)
24	Local.Remote Indicator (Open Collector)
25	Aux 24V+ (150 mA)
13	Aux 24V- (150 mA)

Table 5-1 Input/output designations of Masterflex L/S® Digital Drive [68]

To turn on the remote-control mode of Digital Drive, push the front panel keypad and go to the main menu -> select remote control- >select VOLTAGE INPUT MODE. The VOLTAGE INPUT MODE allowes the user to input a voltage signal to control the flow. The user had an

option to adjust the minimum, maximum and middle setpoints for voltage and flow. In this project, the minimum (MIN) voltage is set to 0.1 V DC. The maximum (MAX) is set to 10.0 V DC, and the flow is set to maximum. The middle (MID) is auto-calculated for a centered voltage and flow between the MIN and the MAX. To confirm VOLTAGE INPUT MODE was selected, select EXIT after returning to the Remote-Control Menu and select CONTINUOUS PUMP MODE.   To deselect Remote Current Input Mode, select LOCAL and ENTER.

5.2.2.3 O_2 gas controller

Figure 5.8 Parker Porter Gas Mass Flow Controllers MPC95

The Porter MASS FLOW CONTROLLER(MFC) MPC95 was employed for the O2 gas flow control. The electrical interface of MFC was connected to the NI USB-6212 Multifunction I/O Device. The analog setpoint voltage input (port 7) (Figure 5.10) and signal ground (port 9) of MFC was connected to port 13 and port 14 (Figure 5.3) of the NI USB-6212, respectively. This couple of connections was for the signal of gas flow control on demand. The analog setpoint voltage output (port 8) and signal ground (port 9) of MFC is connected to port 15 and port 14 of the NI USB-6212, respectively. This couple of connection is for displaying gas flow rate on the control programmer interface.
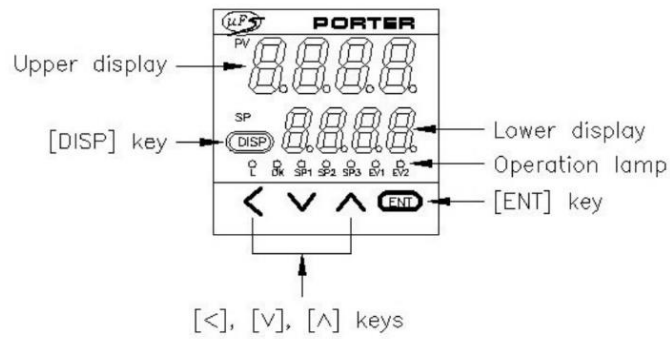
Figure 5.9 Front panel of MFC [69]
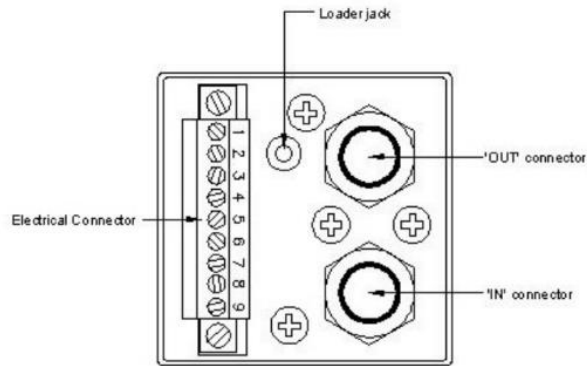
Figure 5.10 Back terminal of MFC [69]

PIN NUMBER	NAME/FUNCTION	DESCRIPTION	COMMENTS
1	POWER (24V)	Power (+24 Vdc)	
2	POWER GND	Power supply ground	
3	EV1	Event output 1	Open collector non-isolated output
4	EV2	Event output 2	
5	DI1	External switch input 1	Switching input (OPEN/GND)
6	DI2	External switch input 2	
7	AI	Analog setpoint voltage input	0 to 5 Vdc or 1 to 5 Vdc (selectable)
8	A0	Analog flow rate voltage output	
9	SIGNAL GND	Signal ground	Input/output signal common. Signal ground is connected with power supply ground within MFC.

Table 5-2 Input/output designations of MPC95 [69]

To turn on the remote-control mode of MFC, press the front panel [DISP] key twice to display

the totalized flow rate, then press [<] key for more than 3 seconds twice until display 'C-01'. Press

either the [∧] or [∨] key until 'C-03'→press the [ENT] key → Press either the [∧] or [∨] key

to select '1' → Press the [ENT] key to store the selected value→ Press the [DISP] key to return to

the instantaneous flow rate display(Figure 5.8).

5.2.2.4 The potentiostat with input and output interface

Figure 5.11 MPG‑220 Bio‑Logic MPG‑220 battery test station

The potentiostat used in this project was a Bio-Logic MPG-220. The MPG-220 provides

auxiliary inputs/outputs (DB9), including voltage /current output, Trigger in, and Trigger out. It

provides a user the ability to control external devices such as a pump and a MFC and to record

external analog signals through the auxiliary DB9 connector.   It can also control and record

analog signals from -10 to + 10 V. The NI USB-6212 Multifunction I/O Device was connected

through DB9-8BNC cable, which conveniently separated the signals to individual end. Then I

monitor BNC (+), and I monitor BNC (-) is connected to port 32 and port 28 (Figure 5.3) of the

NI USB-6212, respectively. This couple of connections is to monitor the current from

potentiostat,. . The details are discussed in a later section. The Trigger out BNC (+) and trigger

out BNC (-) were connected to port 50 and port 49 NI USB-6212 separately. This couple of

connection was for the current measurement range switching from potentiostat. The precision of the current signal depended on the range of measurement. Bio-logic offers a couple of current ranges (Table 3), which all generate 0-1v output signals with different resolutions. For example, a 0.01v output signal would associate to 10mA in a 1 A current range and 1mA in a 100mA current range. Thus, switching the current measurement range would give a better resolution signal to the control module, which reduces the noise significantly. The Trigger in BNC (+) and Trigger in BNC (-) were connected to the port 63 and the port 64 the NI USB-6212, respectively. This couple of connections was to start and stop the potentiostat test through the LabVIEW control interface.

The auxiliary current and voltage monitor signals were automatically activated when the user run experiment methods.   The Trigger in and trigger out were turned on by adding Trigger in and out step (Figure 5.13) in the experiment step sequence.
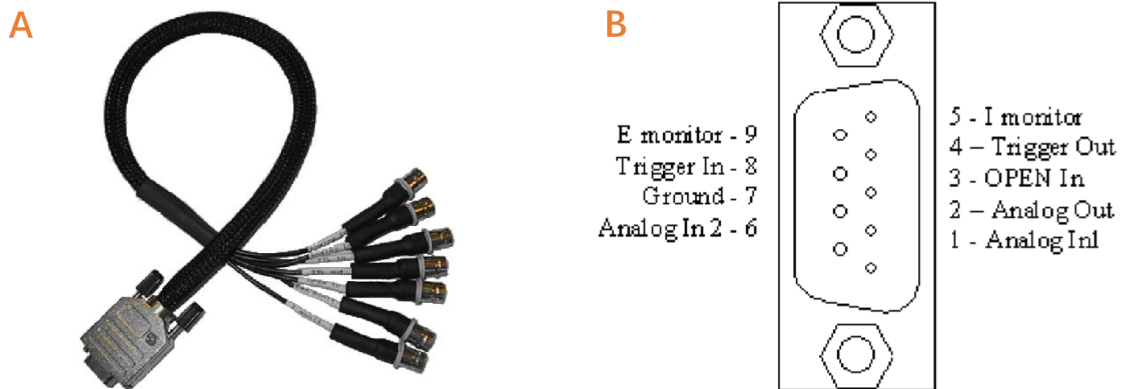
Figure 5.12 DB9-8BNC cable (A) and Structure of the DB9 connector (B) [70]

	Irange	Shunt values	Corresponding voltage range
MPG-2xx	40A	25 mΩ	± 1.0 V
	20A	50 mΩ	± 1.1 V
	10A	100 mΩ	± 1.0 V
	5A	200 mΩ	± 1.1 V
	1A	1 Ω	± 1.0 V
	100 mA	10 Ω	± 1.0 V
	10 mA	100 Ω	± 1.0 V
	1 mA	1 kΩ	± 1.0 V
	100 µA	10 kΩ	± 1.0 V
	10 µA	100 kΩ	± 1.0 V

Table 5-3 The current to voltage conversion table [70]
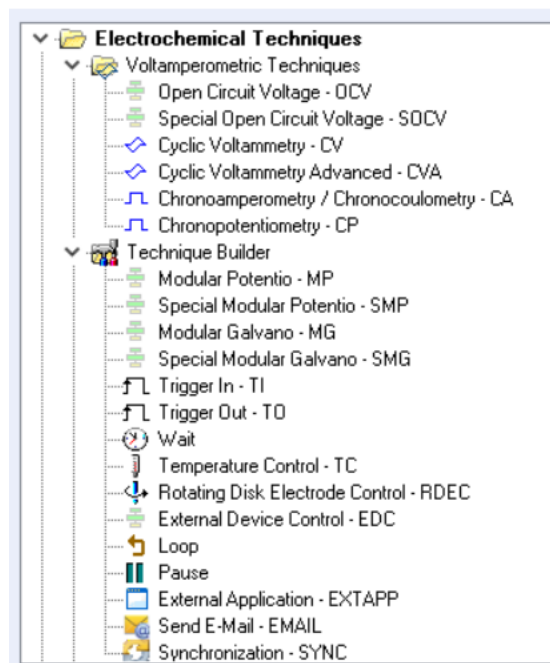
Figure 5.13 Experiment techniques selection

5.2.2.5 PCs

There were two PCs in the system. One is for LabVIEW control , and another was to control Bio-logic potentiostat (EC-Lab software) . The NI-DAQmx driver software (vision 17.6) and LabVIEW 2014 were used. The NI USB 6216 was connected using an USB 2.0 cable. The Bio-logic potentiostat was connected to the desktop through ethernet cable.

5.2.3 Software

The control programming language was LabVIEW 2014. LabVIEW is a general-purpose graphic programming language for control and data acquisitions. It released by National Instruments since 1986. It can be perfectly compatible with any NI hardware. LabVIEW is a highly interactive environment for rapid prototyping, instrument control, and automation applications. It is a revolutionary programming language that depicts program code graphically rather than textually.

LabVIEW programs are called Virtual Instruments (VI). Because it looks very similar the real laboratory instruments. The VI consists of the 'Front Panel' and' block diagram.' The front panel provides the interactive user components like signal display graphs, sliders, buttons, and the dashboard of a virtual instrument. It acts as the front-end of programs. The block diagram was like the circuit board of a real laboratory instrument, which implement logic and algorithm based on the input parameter and output the result to the front panel. The block diagram follows an idea called the 'data flow diagram' concept, where the logic is presented as a diagram rather than programing codes. Typically, a VI consists of one main VI and several sub VI with various functions. This feature makes the program easier to extend and modularized.

5.2.3.1 Front panel
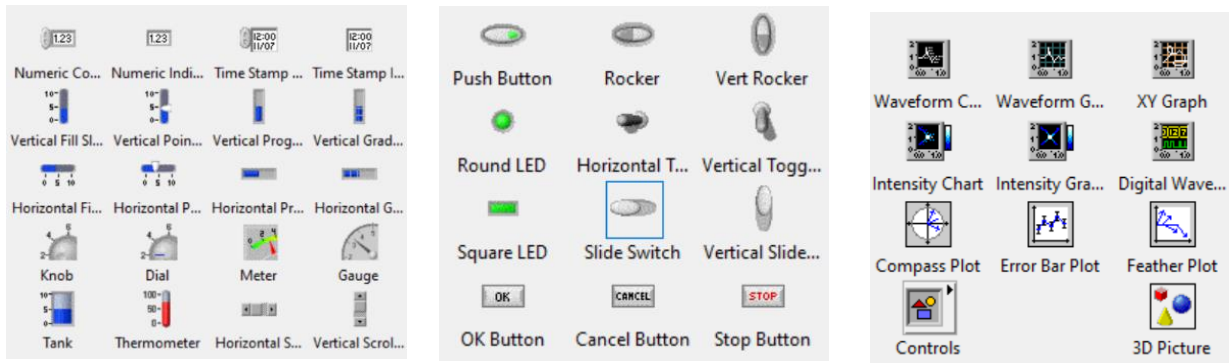
Figure 5.14 The options of the front panel component
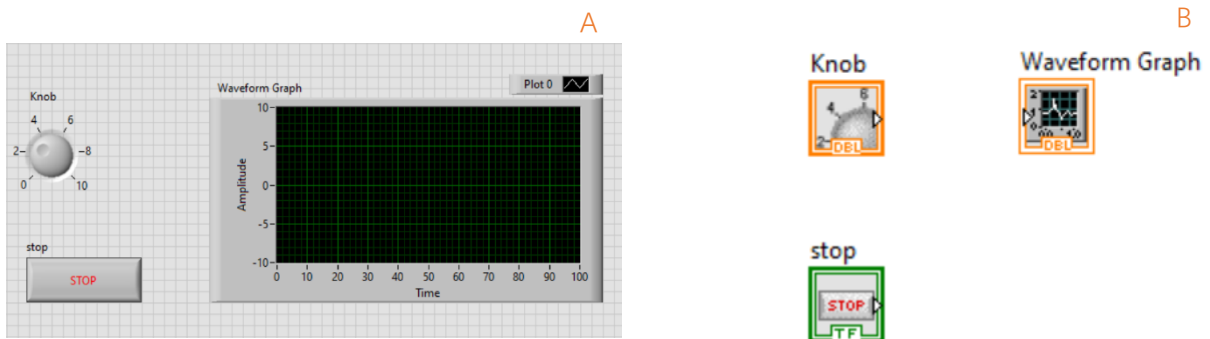
Figure 5.15 Front panel component (A) and block diagram associated terminals (B)

The front panel provides numerous formats to display and input number, Boolean, and signal (Figure 5.14). The way to build the virtual instruments competent is just drag and drop. The user can adjust the components' size and place the competent anywhere on the front panel (Figure 5.15 A). Once the front panel component is created, a terminal is also created at the block diagram (Figure 5.15 B). The terminals act as a pivot between the front panel and block diagram. The terminals represent the data type of the control (Input) or indicator (Output).

5.2.3.2 Block diagram

The block diagram is the core of the program. It consists of a couple of objects to implement an algorism.

5.2.3.2 .1Terminals
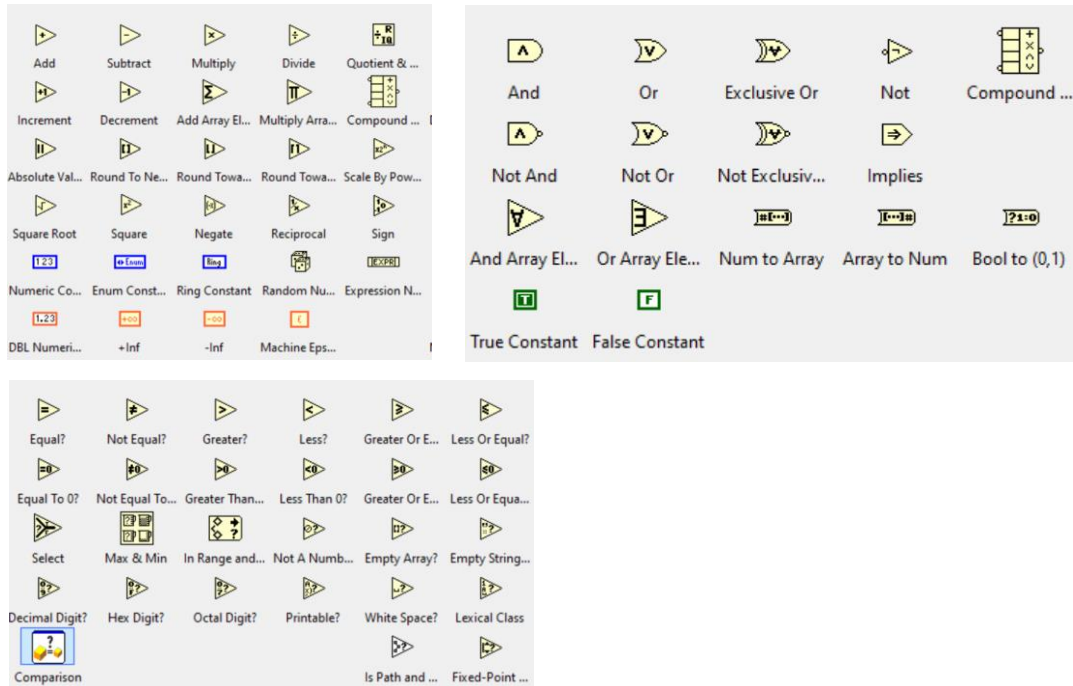
Figure 5.16 The options of Block diagram terminals

The terminals connected to the front panel (Figure 5.14). These objects are the entry and exit ports that facilitate the exchange of information between the front panel and the block diagram. The data that acquired from the instruments enter the block diagram through the control terminals. After the functions complete their calculations in the block diagram, the data flow to the indicator terminals, exit the block diagram, reenter the front panel, and are displayed on the front panel indicators.

5.2.3.2.2 Nodes

The nodes are to perform the numerical and logic calculations. For example, calculate the area

of a circle (Figure 5.17). The results display on the front panel by using indicator terminals. Compare pi and 3.14 (Figure 5.18). If the result is true, the front panel indicator will turn on.

Figure 5.17 A example of numerical calculation
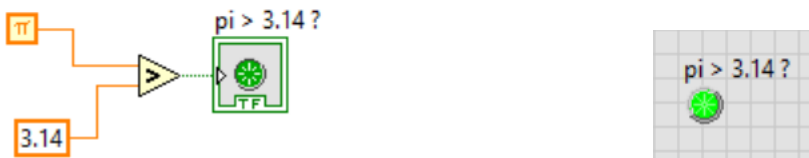
Figure 5.18 A example of logic calculation

5.2.3.2.3 Wires

Data flow between different block diagram objects through wires. Wires could be different colors, styles, and thicknesses, depending on their data types. A broken wire appears as a dashed black line with a red X in the middle, indicating an error between connected two objects. For example, adding numerical value with a Boolean value will be illegal in LabView (Figure 5.19).
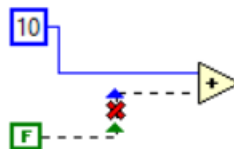
Figure 5.19 A example of wrong connection

Loop and conditional statements are the most typical structures in the programming language. A loop is an instruction that repeats until a specified condition is reached. In a loop structure, the loop asks a question. If the answer requires action, it will be executed. The same question is asked again and again until no further action is required. Each time when the question is asked is called an iteration. A conditional statement is responsible for modifying the flow of execution of a program. The condition is evaluated first before executing any statement. LabVIEW offers a graphical representation of loops and conditional statements (Figure 5.20). Structures are used on the block diagram to repeat blocks of code and to execute code conditionally or in a specific order.
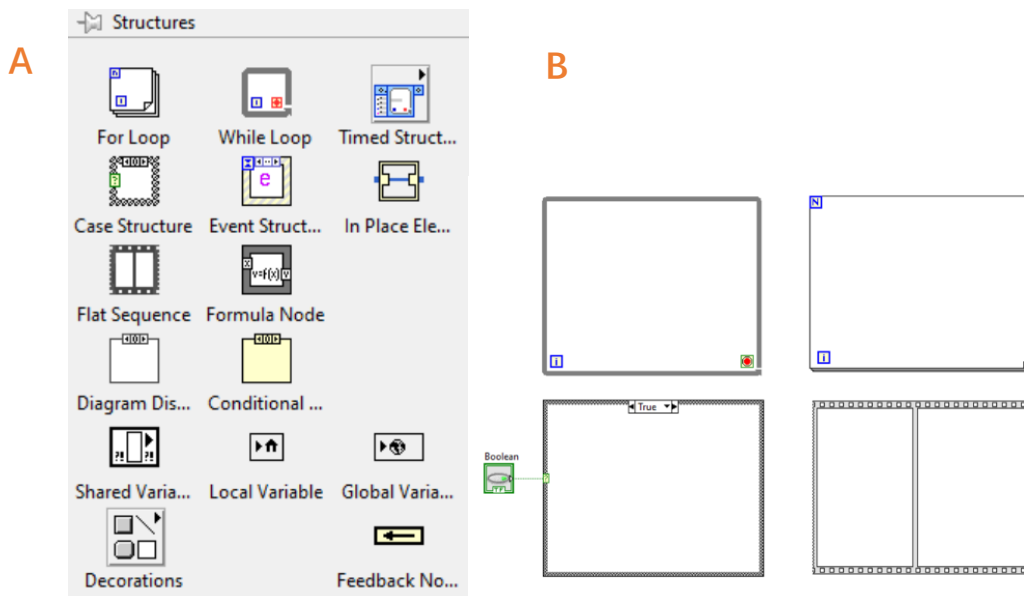
Figure 5.20 The options of structures (A) and the commonly used structures (B)

LabVIEW offers a couple of structures based on program logic. The four most commonly used structures are while loop, for loop, case structure, flat sequence. (Figure 5.20 B). While the loop is executed until the structure's condition is true or false regarding the programming implemented. This structure allows the parallelism of execution. If two while loops are in the same

level of execution, both will be run simultaneously. For loop permits the execution of code for specific times, allowing them to perform an iteration when the number of iteration is known. Case structure allows executing multiple codes based on different cases. If a case type is a Boolean, the case could be considered similar to the if statement. Case structure is the prerequisite of the state machine. The flat sequence permits a sequential execution of the code. The sequences are organized in frames.   The code in each frame waits for the end of the previous one to execute. It could prioritize the code to execute.

5.2.3.2.5 DAQ assistant.

DAQ Assistant is a build-in tool in LabVIEW that guild you through the steps to acquiring sample measurements. It can be an inlet of data acquired from the hardware like NI USB 6216 and outlet of data generated by the LabVIEW VI. This step-by-step assistant can help users set up the data connection between hardware and LabVIEW IV quickly. However, it comes with a limitation of configuration. Once the control configuration becomes complicated, the DAQ assistant might be insufficient. In this project, the DAQ assistant is sufficient for setting up control between various hardware.

To launch the DAQ Assistant, the user needs to create a terminal in the block diagram. The DAQ Assistant located at the Functions palette by going to Measurement I/O >> NI-DAQmx (Figure 5.21). The user can drag and drop the terminal in any location according to the control programmer algorithm. The DAQ Assistant will launch automatically when the user drops the VI on the diagram and open a new task window (Figure 5.22).
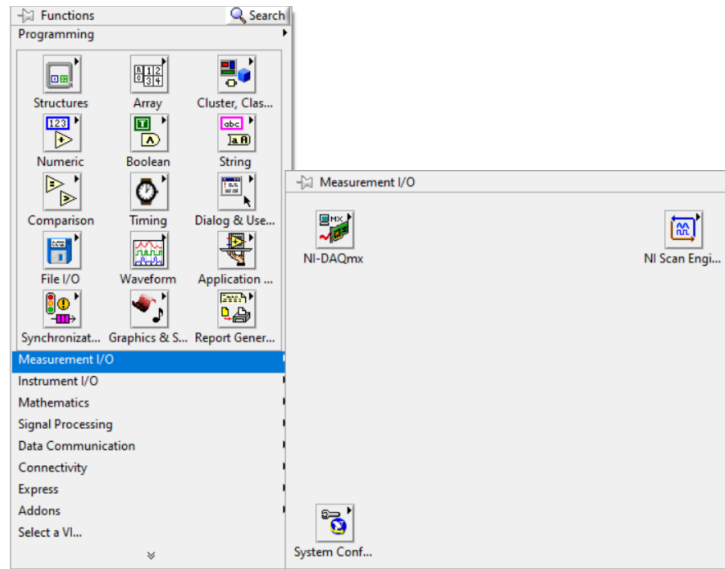
Figure 5.21 Lunch DAQ Assistant
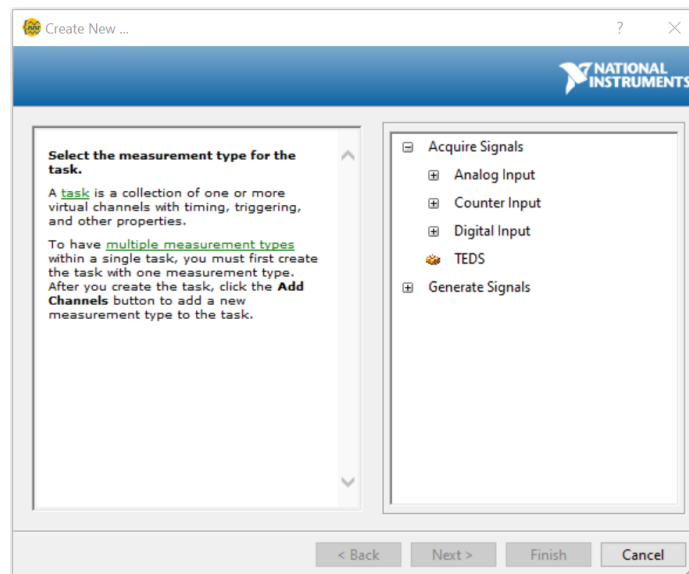
Figure 5.22 The model of DAQ Assistant

In the new task window, the user can select the function of the current DAQ assistant. It could

be the data inlet by choosing to acquire signals or generate signals.   In the subsection of options,

the user could choose various types of signals based on the hardware. The NI USB 6216 is the

complex of analog and digital hardware. Thus, the user could select analog input/output, digital

input/output, or both based on the control programmer algorithm. The next window will show the

user the physical channels of the hardware connected to this PC. The user could select one or multiple channels based on the demand of LabVIEW VI.

Figure 5.23 is the configuration windows. The user can configure channel-specific settings such as scaling, input limits, and terminal configuration. The user also can configure task-specific settings such as timing and triggering. In the connection diagram tap, the user can view the physical port located on the hardware and the right connection way to external hardware.
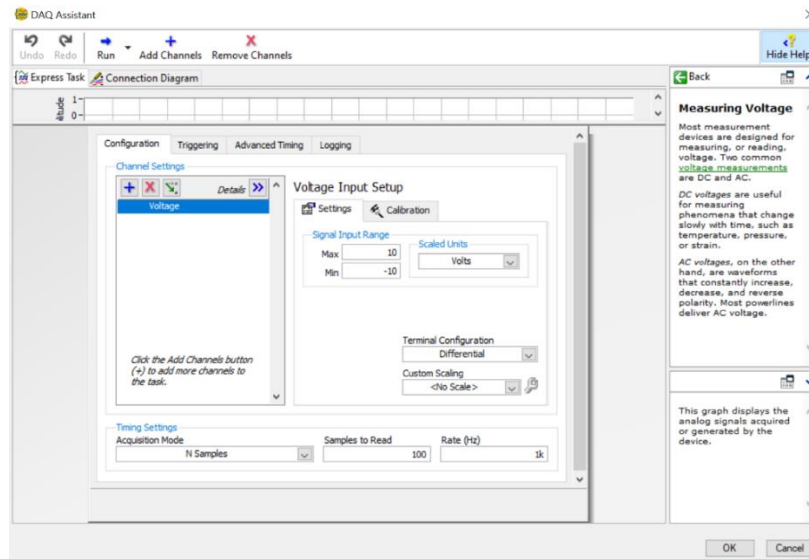
Figure 5.23 Configuration windows of DAQ Assistant

After setting up all parameters of physical connection，the user will have a post configuration terminal (Figure 5.24). The user can link this terminal to other terminals in LabVIEW VI to implement the control function.
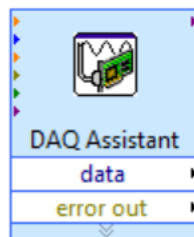
Figure 5.24 Pre-set DAQ Assistant terminal

5.3 Results and discussion

5.3.1 Control VI

The Control VI included one main VI and two SubVIs. The main VI was for main menu options and parameters input and real-time measurement display. The sub VIs includes data input and output from hardware, signal filter, data calculation, state machine on/off.

5.3.1.1 The front panel of main VI

The front panel of the main VI (Figure 5.25) consisted of an input section and a display section. The user could set up each experiment's running time and pump speed when active manual control mode is engaged in the first box in the input section. The second box includes: input of depth of discharge, Zn concentration to the KOH, the current measurement range associated with the potentiostat, the current range switch by automation or manual, and the current offset. The function of those parameters will be discussed in section 3.1.4. The output display section on the right of figure 5.25 includes three graphic display windows. The top one displays the power output of the battery system. The middle one displays the voltage and current real-time. The bottom one displays the calculated flow rate based on the depth of discharge and power output.
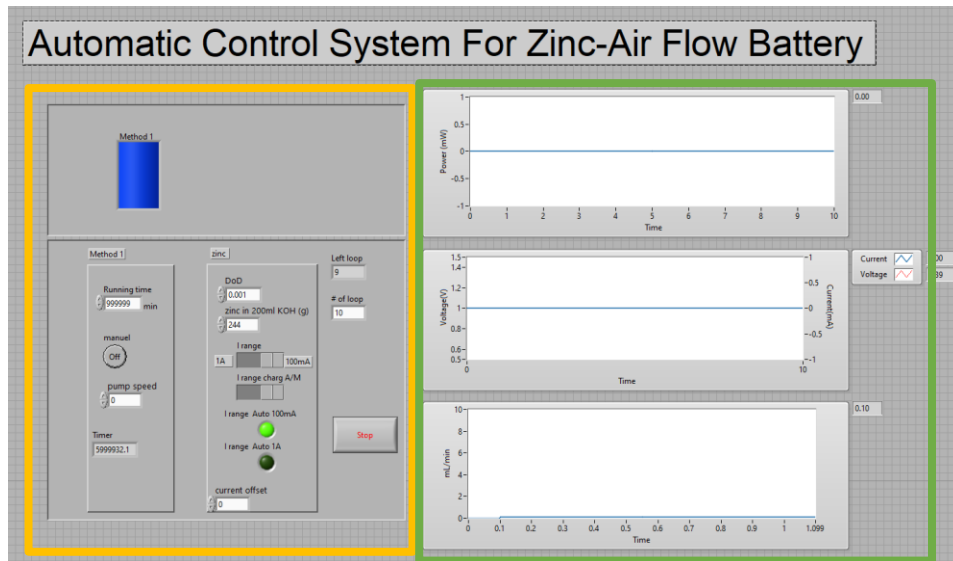
Figure 5.25 The Front panel of main VI
(**input section** and **display section**)

5.3.1.2 The block diagram of the main VI
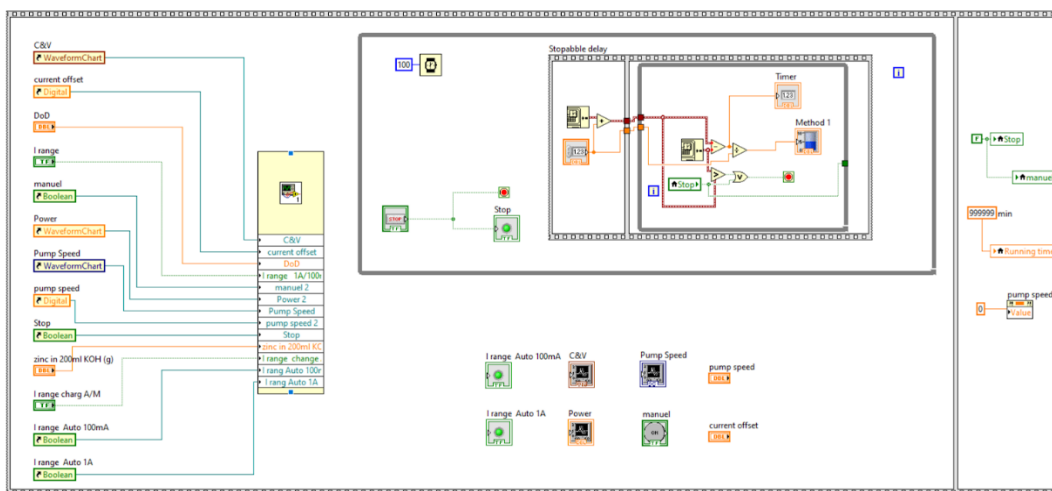
Figure 5.26　The block diagram of main VI

The main components were enclosed in a couple of logical structure. The outermost structure was a flat sequence structure. The flat sequence structure-function was similar to film stock, which provided the order to implement the program's subsection. The first frame of the flat sequence

71

structure included the primary function of the main VI. The second frame included the rest and re-zero of the terminals, which was changed when implementing the first frame, such as the stop button in the front panel (Figure 5.25). When the user hit the stop button, the stop terminals will turn to Ture, which will trigger the loop condition (Figure 5.27) and stop the entire program. However, the stop terminal would keep Ture state when users restarted the program while leading the program to stop immediately. In order to avoid this, a reset of the stop button terminal is needed at the end of the program.

There were three major blocks inside the first fame of flat sequence structure (Figure 5.26). The first one is while loop structure, which plays the role of letting the program repeat until the stop condition was reached (Figure 5.27). Two conditions can stop the program. The first one is the stop button, and the second is time out. There is a time out stop implemented by a flat sequence structure with a while loop. The algorithm of time out stops is comparing the setting time with the current time. If the current time is great than setting time, trigger the time out stop. The second block is the physical terminal of input and display component in the front panel (Figure 5.28). The terminals are the data input/output node that interreacts with other terminals or VI.
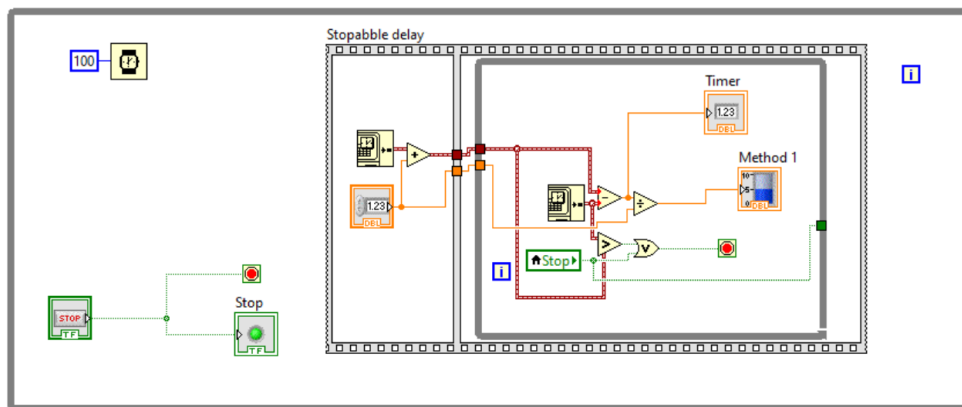
Figure 5.27 The loop structure in the main VI

72

Figure 5.28 The terminals for input and display component

The third block is a subVI linked with reference of the input/output terminal（Figure 5.29）

LabVIEW can link to subVIs by two different methods, static and dynamic. If the physical terminal in second block links with subVI, it will create a statically linked subVI.It is loaded into memory at the same time the main VI is loaded. Thus, the program only takes the preset parameter before running. The user cannot change the parameter during the program going. In order to make the program more interactivity, dynamic linking is employed. With dynamic linking, subVIs are not loaded until specifically instructed by the code of the main VI. This enables the programmer to create programs that take less memory and real-time interacted.
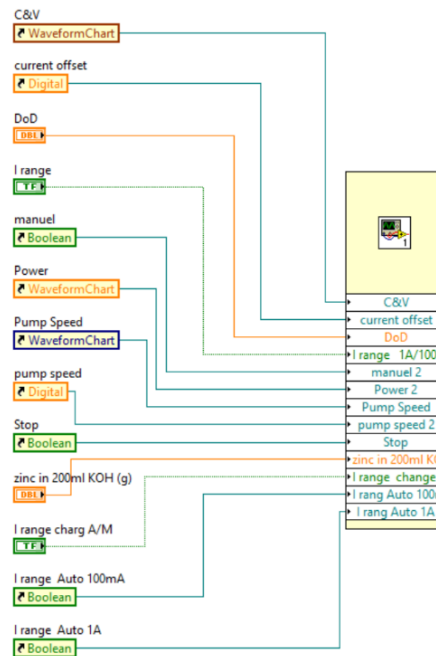
Figure 5.29 The subVI(1) terminal in main VI

5.3.1.3 The sub VI (1)
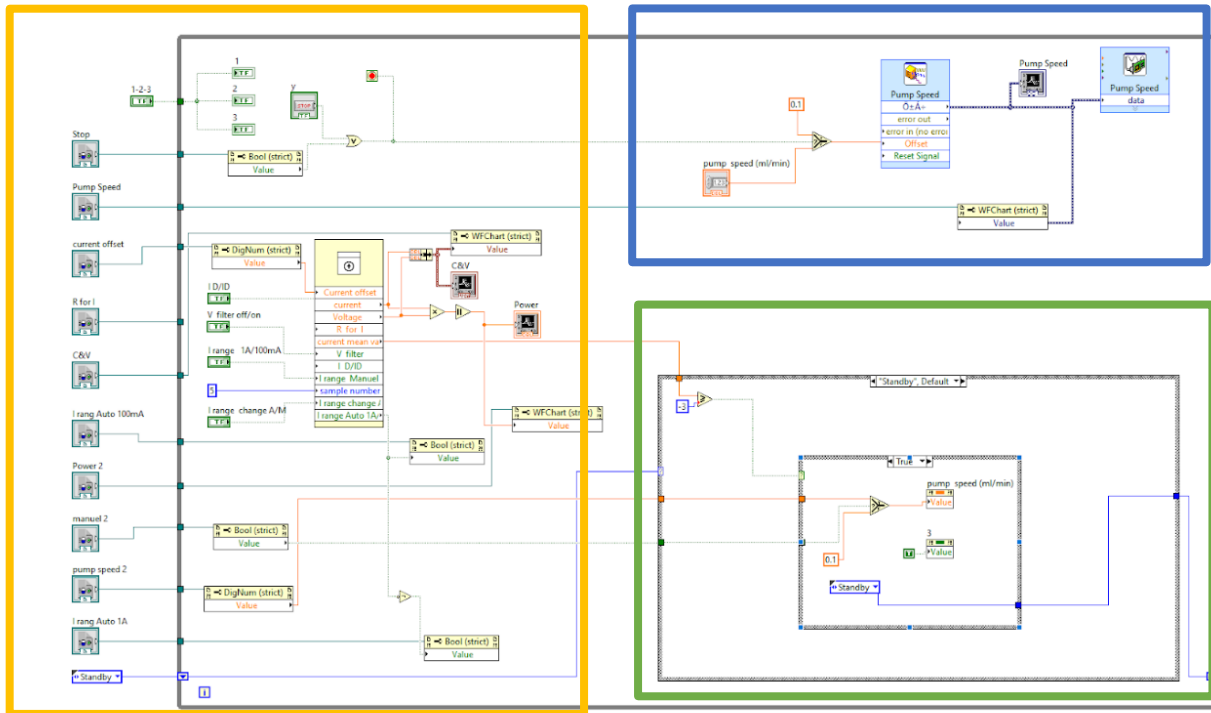
Figure 5.30 The block diagram of sub VI（1）
(**data acquisition and procession section**, **control signal generation section,** and **control algorithm implementation section.**)

SubVI(1) is the core of the program. It consists of data acquisition and procession section, control signal generation section, and control algorithm implementation section. (Figure 5.30)

The three sections are enclosed in a while loop structure, which plays the role of repeating the program until the stop condition has been reached. Two conditions can stop the program. The first one is the stop button in SubVI(1) and the stop button in main VI. The data acquisition and procession section are packed into subVI(2) and linked with reference of the input/output terminal. This section takes the procession parameters from main VI and collects and processes raw data from NI USB-6212 interface. The detail will be discussed in the next section.

The control signal generation section controls the speed of the peristaltic pump. The peristaltic

pump's speed is proportional to the voltage output from the NI USB-6212 interface by using VOLTAGE INPUT MODE of the pump. The voltage output signal is the DC signal generated by the built-in signal simulate VI. The magnitude of the DC signal is controlled by the offset, numerical data from the control algorithm implementation section. The mixed DC signal flows to pump speed DAQ Assistant, configure as analogy output of NI USB-6212 interface.   The control algorithm implementation section fulfills the fundamental idea of the zinc-air flow battery system. The basic structure of this section is a state machine (Figure 5.31). The states machine receives the current data from the data acquisition and procession section and adjusts the states based on the current range. There are three states, Max speed, controlled speed, and standby in this state machine.
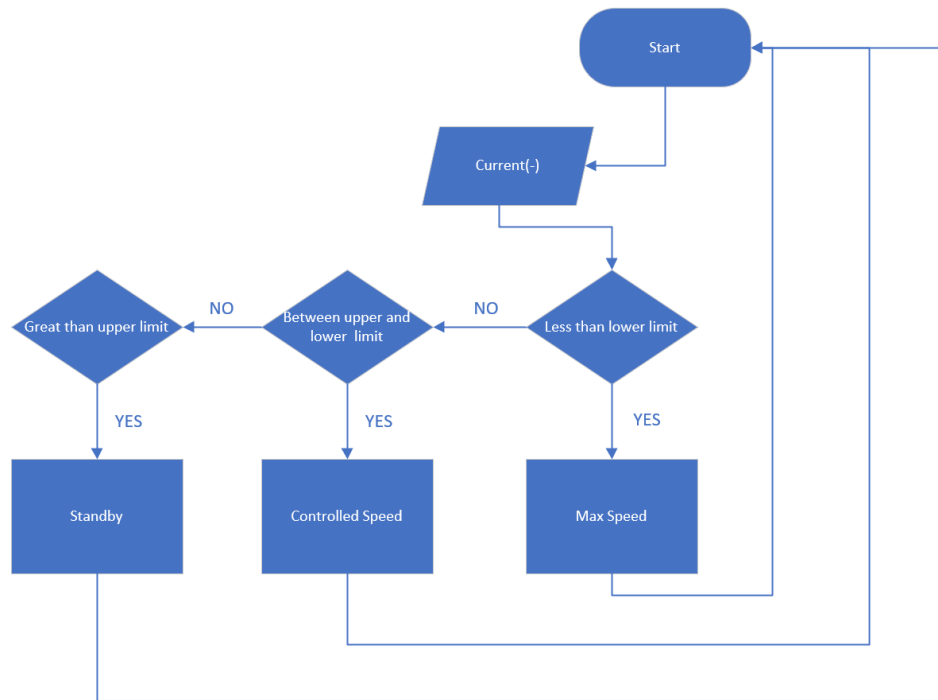
Figure 5.31 The state machine schematic

The Max speed state is when the output current of the battery goes above the max current the cell could desire to provide. The battery ideally operates below a Max flow rate since internal resistance will increase if above that. The Max flow rate would vary based on the target DoD and electrode material density, which the parameter set at the main VI front panel. Once the current goes above the limitation, the pump will keep the maximum speed no matter how the current increase, which means the DOD will not be sustained. The Max speed state is a worse scenario when battery discharge, which will cause the heavily nonuniform DoD of the electrode material. Typically, the battery should keep away from this state. However, there is a short pulse current during battery discharge. The Max speed state could keep internal resistance relatively low, so the voltage would not drop rapidly. The controlled speed state is the core of this section. It implements the algorithm in which the discharge current's flow rate is controlled to keep the DoD constant. The constant DoD will make sure the zinc particle morphology uniform as much as possible, which is a critical point to recharge the battery. The mass and energy balance calculations will be discussed in a later section.   The standby state ensures the zinc slurry electrode flowing with the lowest speed, which offset the zinc particle settlement due to gravity. A case structure builds the state machine. The case structure is a unique structure in LabVIEW and perfect march the need of state machine, which is closed to the if-else or switch-case structure in another programming language. Each state of a state machine can be represented as a case, and the program can determine which state will go to the next step according to the real-time calculation.

5.3.1.4 The sub VI (2)

Sub VI (2) is a module in the data acquisition and procession section of sub VI (1) (Figure 5.30). The data acquisition includes digital signal input and analogy input. The digital signal input

DAQ assistant links to the NI USB-6212 port 50, which is connected to the trigger out BNC of potentiostat. This digital input signal is for the current measurement range switching from potentiostat. The precision of the current signal depended on the range of measurement. The analogy signal input DAQ assistant links to the NI USB-6212 port 32, port 31 and port 28(Figure 5.3), which are connected to current and voltage measurement resource. The port 32 is assigned to connect the current monitor BNC of the potentiostat, which generates ±1 V voltage signal (Table 3) to represent current measurement. This current resource is the indirect measurement, which must use potentiostat or other current measurement instruments. The port 31 is assigned to connect them directly with the current measurement resource from the battery. Using a fixed value shunt in the battery test circuit and testing the two sides of a shunt's voltage response, the current could be measured directly. The direct current measurement does not need current measurement instruments like potentiostat. However, it comes with a high level of thermal noise. To reduce the noise, a LabVIEW built-in signal filter is employed in the data process part. The port 28 could be either connected to voltage monitor BNC of potentiostat or two sides of the battery to measure voltage.

The data process plays a critical role in smoothing the input signal and pass the processed data to the next section. It has the function of switching different measurement ranges, filtering the signal noise, and smooth the data. When an instrument indirectly measures the current, the current range could affect the signal's resolution. For example, the Bio-logic MPG-220 potentiostat use 0-1v to represent 0-1A and 0-100mA at different measurement range. The 50mA would convert to 0.05v at 0-1A range and 0.5v at 0-100mA range. The Signal-to-Noise Ratio of 0.5v is 10x higher than 0.05v due to signal resolution. Moreover, another issue is that the instrument will not provide reliable output data once the current goes above the measurement range. To solve those problems,

the current range switching according to the current output is necessary when designing the tests' workflow in potentiostat. Once the current range is switched, the numerical value output voltage data will represent different currents. So, the potentiostat has to talk with VI in terms of the current range. The subVI（2）provides auto and manual two options to recognize the current range. The auto option requires a trigger in single, which generate by the potentiostat. If the external instrument does not have features to generate a trigger in the signal, the user could manually set the current range. When the current measurement in the direct model, the thermal noise comes from the shunt is significantly affecting the quality of the input signal. A LabVIEW built-in low-pass filter is employed to reduce the thermal noise. A low-pass filter is to pass low moving signals (low frequency), but it stops signals with high frequencies. This is the most common way of improving the analogy signal. The entire data acquisition and procession section are enclosed in the For-loop structure, which repeats the terminals inside the loop for a specific time then stop. The gold of using a for-loop structure is for applying a moving average to smooth the signal. The smoothed signal will reduce the control stress of the state machine. Off cause, it will cause lagging and drifty, so the tune in the moving average span is necessary to balance the benefit and loss.

I monitor BNC (+), and I monitor BNC (-) is connected to port 32 of NI USB-6212 separately. This couple of connections is to monitor the current from potentiostat, which is indirectly current measurement.
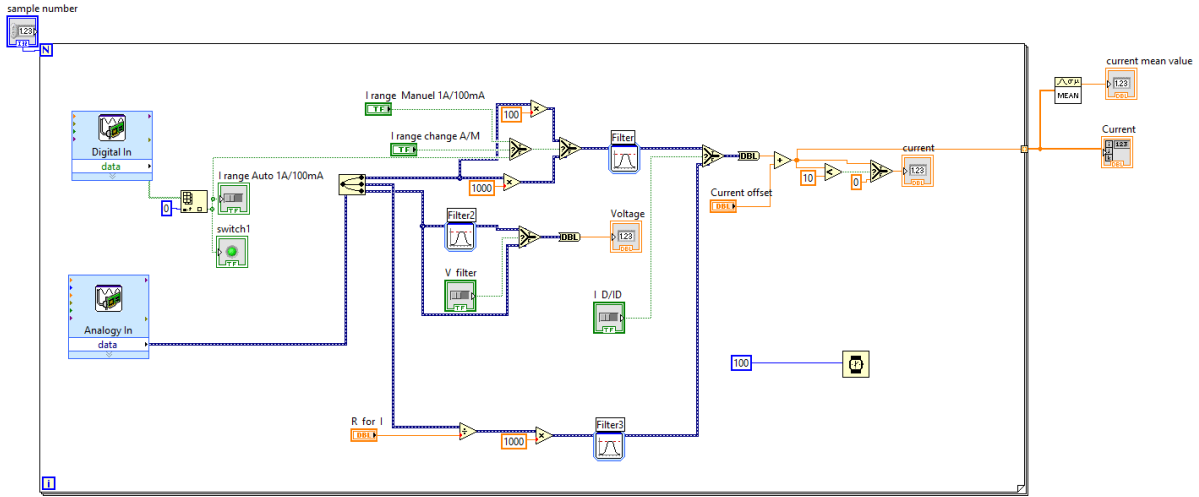
Figure 5.32 The block diagram of the sub VI（2）

5.3.2 Control algorithm

The core idea of the zinc-air flow battery is keeping the DoD constant according to current demand. Thus, the control algorithm's fundamental is to match the discharge current with zinc slurry electrode flow rate.

The flowing equations can describe how does it work

$$I = dQ/dt \qquad (1)$$

$$Q = m_{zn}/M_{zn} * N_e * F * DoD \qquad (2)$$

$$\dot{m}_{zn} = dm_{zn}/dt \qquad (3)$$

$$\dot{v}_{slurry} = \dot{m}_{zn}/\rho_{eff} \qquad (4)$$

Thus

$$\dot{v}_{slurry} = \frac{I*M_{zn}}{N_e*F*DoD*\rho_{eff}} \qquad (5)$$

Where I is the current

Q is Coulomb

m_{zn} is mass of zinc

M_{zn} is molar mass of zinc

N_e is electron transferred in the reaction

F is faraday constant

DoD   is depth of discharge

$\dot{m}_{zn}$ is mass flow rate of raw zinc

$\dot{v}_{slurry}$ is volumetric flow rate of zinc slurry

ρ_{eff} is effective density of zinc slurry

Those algorithm equations are based on two assumptions: the volume change of zinc slurry is negligible, and the raw zinc volume is much smaller than the KOH gel electrolyte. The effective density of zinc slurry equates mass of raw zinc/volume of KOH gel electrolyte. However, the effective density will change if zinc is discharged to high DoD. Excessive ZnO will also affect the effective density of zinc slurry. Thus, the equation tune-in, according to the DoD and effective density, is necessary for future work.

5.4 Conclusion

The zinc-air flow battery system is a complex of the battery and battery management system (BMS). The BMS can make sure the battery operating at an optimized DoD range so that the battery could be charged without dendrite formation and anode material shape changing.

In this chapter, a LabVIEW based BMS is discussed. The BMS included software (LabVIEW) and hardware (NI Multifunction I/O Device). The VI (software) is made of one main VI and two subVIs. The main VI 's function is options and parameter input and real-time measurement display. The subVI(1) included data acquisition and procession section, control signal generation section, and control algorithm implementation section. The subVI (2) is a module in the data acquisition and procession section of subVI (1). The multifunction I/O device is connected to a controllable peristaltic pump, a O2 Gas CONTROLLER, a potentiostat(or battery in direct mode), and a PC. The control algorithm and the mathematic equations are introduced as well.

Chapter 6 Summary and Future Work

The zinc-air flow battery system is a novel energy storage application combined with the advantages of both a zinc-air battery and a redox flow battery. The combination permits the zinc-air flow battery to compete with the current leading battery technologies in the marketplace.

A rechargeable Zn-air flow battery with an automatic control system was designed and prototyped in our previous researches. In this study, the Zn-air flow battery system has been investigated and optimized.

The reactor was re-designed, so the issues of the non-reacted "dead zinc" and the deformation of the air cathode were addressed. Benefited from the use of the additive manufacturing process (3D print), the reactor's performance was tripled. The PTFE was selected against PVC as the material of the reactor body, since it provided better cell performance in terms of the low cell impedance, the reduction of clogging, and the decline of the electrolyte creepage. The anode current collector and flow field design were also investigated and optimized.   The metal 3D anode current collector demonstrated excel performance over 2D anode current collector. The flow field is still needed to be further studied to reduce clogging.

The parameters of air cathode fabrication were researched, including the thickness, the binder content, and the expanded graphite content of the active layer. The 0.2mm was chosen as the desired thickness considering the efficiency of material and the easiness of fabrication. The PTFE content was 5%, and expanded graphite content was 10% in the catalyst layer to balance balancing the electronic conductivity and tenacity.   The thickness of the current corrector, the selection of GDL, the hot press's temperature, and the method to reinforce the connection between

different layers would be a high priority in the next phase study.

The algorithm and design of a LabVIEW based battery management system (BMS) was discussed in chapter 5. The BMS is fully functional to implement the control algorithm; which is to keep a constant DoD constant according to the power demand. The BMS includes software (LabVIEW) and hardware (NI Multifunction I/O Device). The multifunction I/O device is connected to a controllable peristaltic pump, an O_2 gas controller, a potentiostat in indirect mode (or battery in direct mode), and a PC. The PID controller integration , the noise reduction by a physical filter, multiple-cells BMS would be the area in the next phase study.

There are still a few things challenge to be investigated in the future study, like Zinc slurry anode making and optimization, regenerator design, the issue associated with the system scale up, the layout of cells in parallel or in serious.

REFERENCES

1.   Institute, E. E. Electric Vehicle Sales: Facts & Figures 2019. InsideEVs.com.

2.   ev-database. 2020.

3.   Patrick Hertzke, N. M., Patrick Schaufuss, Stephanie Schenk, and Ting Wu. Expanding electric-vehicle adoption despite early growing pains 2019.

4.   RESEARCH, C. A. D. What is Average Mileage Per Year? 2020. https://www.caranddriver.com/research/a32880477/average-mileage-per-year/.

5.   Chen, H. S.;   Cong, T. N.;   Yang, W.;   Tan, C. Q.;   Li, Y. L.; Ding, Y. L., Progress in electrical energy storage system: A critical review. *Prog Nat Sci* **2009,** *19* (3), 291-312.

6.   What is U.S. electricity generation by energy source? **2019**.

7.   Gür, T. M., Review of electrical energy storage technologies, materials and systems: challenges and prospects for large-scale grid storage. *Energ Environ Sci* **2018,** *11* (10), 2696-2767.

8.   Argyrou, M. C.;   Christodoulides, P.; Kalogirou, S. A., Energy storage for electricity generation and related processes: Technologies appraisal and grid scale applications. *Renew Sust Energ Rev* **2018,** *94*, 804-821.

9.   Ellabban, O.;   Abu-Rub, H.; Blaabjerg, F., Renewable energy resources: Current status, future prospects and their enabling technology. *Renew Sust Energ Rev* **2014,** *39*, 748-764.

10.   Agency, I. R. E., REthinking Energy 2017 : Accelerating the global energy transformation. **2017**.

11.   Si, J. Development of an Advanced Zinc Air Flow Battery System. University of Massachusetts Boston, 2017.

12.   Cheng, F.; Chen, J., Metal-air batteries: from oxygen reduction electrochemistry to cathode catalysts. *Chem Soc Rev* **2012,** *41* (6), 2172-92.

13. Liu, Q. C.; Chang, Z. W.; Li, Z. J.; Zhang, X. B., Flexible Metal-Air Batteries: Progress, Challenges, and Perspectives. *Small Methods* **2018,** *2* (2).

14. Menictas, C.; Skyllas-Kazacos, M.; Lim, T. M., *Advances in Batteries for Medium and Large-Scale Energy Storage: Types and Applications*. Elsevier Science: 2014.

15. Sun, Y. T.; Liu, X. R.; Jiang, Y. M.; Li, J.; Ding, J.; Hu, W. B.; Zhong, C., Recent advances and challenges in divalent and multivalent metal electrodes for metal-air batteries. *J Mater Chem A* **2019,** *7* (31), 18183-18208.

16. Fu, J.; Cano, Z. P.; Park, M. G.; Yu, A.; Fowler, M.; Chen, Z., Electrically Rechargeable Zinc-Air Batteries: Progress, Challenges, and Perspectives. *Adv Mater* **2017,** *29* (7).

17. Chawla, N., Recent advances in air-battery chemistries. *Materials Today Chemistry* **2019,** *12*, 324-331.

18. Zhang, J.; Zhou, Q.; Tang, Y.; Zhang, L.; Li, Y., Zinc-air batteries: are they ready for prime time? *Chem Sci* **2019,** *10* (39), 8924-8929.

19. Fu, J.; Liang, R.; Liu, G.; Yu, A.; Bai, Z.; Yang, L.; Chen, Z., Recent Progress in Electrically Rechargeable Zinc-Air Batteries. *Adv Mater* **2019,** *31* (31), e1805230.

20. Liu, Y. W.; Xiao, C.; Lyu, M. J.; Lin, Y.; Cai, W. Z.; Huang, P. C.; Tong, W.; Zou, Y. M.; Xie, Y., Ultrathin Co3S4 Nanosheets that Synergistically Engineer Spin States and Exposed Polyhedra that Promote Water Oxidation under Neutral Conditions. *Angew Chem Int Edit* **2015,** *54* (38), 11231-11235.

21. Mabayoje, O.; Shoola, A.; Wygant, B. R.; Mullins, C. B., The Role of Anions in Metal Chalcogenide Oxygen Evolution Catalysis: Electrodeposited Thin Films of Nickel Sulfide as "Pre-catalysts". *ACS Energy Letters* **2016,** *1* (1), 195-201.

22. Wu, M.; Wang, Y.; Wei, Z.; Wang, L.; Zhuo, M.; Zhang, J.; Han, X.; Ma, J., Ternary doped porous carbon nanofibers with excellent ORR and OER performance for zinc–air batteries. *J Mater Chem A* **2018,** *6* (23), 10918-10925.

23. Zeng, M.; Liu, Y.; Zhao, F.; Nie, K.; Han, N.; Wang, X.; Huang, W.; Song, X.; Zhong, J.; Li, Y., Metallic Cobalt Nanoparticles Encapsulated in Nitrogen-Enriched Graphene Shells: Its Bifunctional Electrocatalysis and Application in Zinc-Air Batteries. *Advanced Functional Materials* **2016,** *26* (24), 4397-4404.

24. Ai, L.; Tian, T.; Jiang, J., Ultrathin Graphene Layers Encapsulating Nickel Nanoparticles Derived Metal–Organic Frameworks for Highly Efficient Electrocatalytic Hydrogen and Oxygen Evolution Reactions. *ACS Sustainable Chemistry & Engineering* **2017,** *5* (6), 4771-4777.

25. Chen, X.; Liu, B.; Zhong, C.; Liu, Z.; Liu, J.; Ma, L.; Deng, Y.; Han, X.; Wu, T.; Hu, W.; Lu, J., Flexible Batteries: Ultrathin Co3

O4

 Layers with Large Contact Area on Carbon Fibers as High-Performance Electrode for Flexible Zinc-Air Battery Integrated with Flexible Display (Adv. Energy Mater. 18/2017). *Advanced Energy Materials* **2017,** *7* (18).

26. Wang, G. W.; Zheng, D.; Liu, D.; Harris, J.; Si, J. Y.; Ding, T. Y.; Qu, D. Y., Highly Efficient Ni-Fe Based Oxygen Evolution Catalyst Prepared by A Novel Pulse Electrochemical Approach. *Electrochim Acta* **2017,** *247*, 722-729.

27. Cano, Z. P.; Park, M. G.; Lee, D. U.; Fu, J.; Liu, H.; Fowler, M.; Chen, Z., New Interpretation of the Performance of Nickel-Based Air Electrodes for Rechargeable Zinc–Air Batteries. *The Journal of Physical Chemistry C* **2018,** *122* (35), 20153-20166.

28. Mainar, A. R.; Colmenares, L. C.; Blázquez, J. A.; Urdampilleta, I., A brief overview of secondary zinc anode development: The key of improving zinc-based energy storage systems. *International Journal of Energy Research* **2018,** *42* (3), 903-918.

29. Parker, J. F.; Chervin, C. N.; Nelson, E. S.; Rolison, D. R.; Long, J. W., Wiring zinc in three dimensions re-writes battery performance-dendrite-free cycling. *Energ Environ Sci* **2014,** *7* (3), 1117-1124.

30. Gan, W. G.;　Zhou, D. B.;　Zhou, L.;　Zhang, Z. J.; Zhao, J., Zinc electrode with anion conducting polyvinyl alcohol/poly(diallyldimethylammonium chloride) film coated ZnO for secondary zinc air batteries. *Electrochim Acta* **2015,** *182*, 430-436.

31. Higashi, S.;　Lee, S. W.;　Lee, J. S.;　Takechi, K.; Cui, Y., Avoiding short circuits from zinc metal dendrites in anode by backside-plating configuration. *Nat Commun* **2016,** *7*, 11801.

32. Qi, Z. X.; Koenig, G. M., Review Article: Flow battery systems with solid electroactive materials. *J Vac Sci Technol B* **2017,** *35* (4).

33. Gandomi, Y. A.;　Aaron, D. S.;　Houser, J. R.;　Daugherty, M. C.;　Clement, J. T.;　Pezeshki, A. M.;　Ertugrul, T. Y.;　Moseley, D. P.; Mench, M. M., Critical Review-Experimental Diagnostics and Material Characterization Techniques Used on Redox Flow Batteries. *J Electrochem Soc* **2018,** *165* (5), A970-A1010.

34. Perry, M. L.; Weber, A. Z., Advanced Redox-Flow Batteries: A Perspective. *J Electrochem Soc* **2016,** *163* (1), A5064-A5067.

35. Ye, R. J.;　Henkensmeier, D.;　Yoon, S. J.;　Huang, Z. F.;　Kim, D. K.;　Chang, Z. J.;　Kim, S.; Chen, R. Y., Redox Flow Batteries for Energy Storage: A Technology Review. *J Electrochem Energy* **2018,** *15* (1).

36. Skyllas-Kazacos, M.; Limantari, Y., Kinetics of the chemical dissolution of vanadium pentoxide in acidic bromide solutions. *J Appl Electrochem* **2004,** *34* (7), 681-685.

37. Skyllas-Kazacos, M., Novel vanadium chloride/polyhalide redox flow battery. *J Power Sources* **2003,** *124* (1), 299-302.

38. Huskinson, B.;　Marshak, M. P.;　Suh, C.;　Er, S.;　Gerhardt, M. R.;　Galvin, C. J.;　Chen, X.;　Aspuru-Guzik, A.;　Gordon, R. G.; Aziz, M. J., A metal-free organic-inorganic aqueous flow battery. *Nature* **2014,** *505* (7482), 195-8.

39. Yang, B.;　Hoober-Burkhardt, L.;　Wang, F.;　Prakash, G. K. S.; Narayanan, S. R., An Inexpensive Aqueous Flow Battery for Large-Scale Electrical Energy Storage Based on Water-Soluble Organic Redox Couples. *J Electrochem Soc* **2014,** *161* (9), A1371-A1380.

40. Matsuda, Y.; Tanaka, K.; Okada, M.; Takasu, Y.; Morita, M.; Matsumurainoue, T., A Rechargeable Redox Battery Utilizing Ruthenium Complexes with Non-Aqueous Organic Electrolyte. *J Appl Electrochem* **1988,** *18* (6), 909-914.

41. Xie, Z.; Liu, Q.; Chang, Z.; Zhang, X., The developments and challenges of cerium half-cell in zinc–cerium redox flow battery for energy storage. *Electrochim Acta* **2013,** *90*, 695-704.

42. Li, Z.; Pan, M. S.; Su, L.; Tsai, P. C.; Badel, A. F.; Valle, J. M.; Eiler, S. L.; Xiang, K.; Brushett, F. R.; Chiang, Y. M., Air-Breathing Aqueous Sulfur Flow Battery for Ultralow-Cost Long-Duration Electrical Storage. *Joule* **2017,** *1* (2), 306-327.

43. Duduta, M.; Ho, B.; Wood, V. C.; Limthongkul, P.; Brunini, V. E.; Carter, W. C.; Chiang, Y.-M., Semi-Solid Lithium Rechargeable Flow Battery. *Advanced Energy Materials* **2011,** *1* (4), 511-516.

44. Zhu, C.; Liu, T. Y.; Qian, F.; Chen, W.; Chandrasekaran, S.; Yao, B.; Song, Y.; Duoss, E. B.; Kuntz, J. D.; Spadaccini, C. M.; Worsley, M. A.; Li, Y., 3D printed functional nanomaterials for electrochemical energy storage. *Nano Today* **2017,** *15*, 107-120.

45. Ngo, T. D.; Kashani, A.; Imbalzano, G.; Nguyen, K. T. Q.; Hui, D., Additive manufacturing (3D printing): A review of materials, methods, applications and challenges. *Compos Part B-Eng* **2018,** *143*, 172-196.

46. Ambrosi, A.; Moo, J. G. S.; Pumera, M., Helical 3D-Printed Metal Electrodes as Custom-Shaped 3D Platform for Electrochemical Devices. *Advanced Functional Materials* **2016,** *26* (5), 698-703.

47. Liu, X.; Jervis, R.; Maher, R. C.; Villar-Garcia, I. J.; Naylor-Marlow, M.; Shearing, P. R.; Ouyang, M.; Cohen, L.; Brandon, N. P.; Wu, B., 3D-Printed Structural Pseudocapacitors. *Advanced Materials Technologies* **2016,** *1* (9).

48. Ye, L. H.; Wen, K. C.; Zhang, Z. X.; Yang, F.; Liang, Y. C.; Lv, W. Q.; Lin, Y. K.; Gu, J. M.; Dickerson, J. H.; He, W. D., Highly Efficient Materials Assembly Via Electrophoretic Deposition for Electrochemical Energy Conversion and Storage Devices. *Advanced Energy Materials* **2016,** *6* (7).

49. Huang, Y.;   Liu, H.;   Lu, Y. C.;   Hou, Y. L.; Li, Q., Electrophoretic lithium iron phosphate/reduced graphene oxide composite for lithium ion battery cathode application. *J Power Sources* **2015,** *284*, 236-244.

50. Yang, Y.;   Chen, D.;   Liu, B.; Zhao, J., Binder-free Si nanoparticle electrode with 3D porous structure prepared by electrophoretic deposition for lithium-ion batteries. *ACS Appl Mater Interfaces* **2015,** *7* (14), 7497-504.

51. Wang, S. L.;   Huang, Z. C.;   Li, R.;   Zheng, X.;   Lu, F. X.; He, T. B., Template-assisted synthesis of NiP@CoAl-LDH nanotube arrays with superior electrochemical performance for supercapacitors. *Electrochim Acta* **2016,** *204*, 160-168.

52. Pikul, J. H.;   Gang Zhang, H.;   Cho, J.;   Braun, P. V.; King, W. P., High-power lithium ion microbatteries from interdigitated three-dimensional bicontinuous nanoporous electrodes. *Nat Commun* **2013,** *4*, 1732.

53. Zhang, F.;   Wei, M.;   Viswanathan, V. V.;   Swart, B.;   Shao, Y.;   Wu, G.; Zhou, C., 3D printing technologies for electrochemical energy storage. *Nano Energy* **2017,** *40*, 418-431.

54. Xu, Y. F.;   Hennig, I.;   Freyberg, D.;   Strudwick, A. J.;   Schwab, M. G.;   Weitz, T.; Cha, K. C. P., Inkjet-printed energy storage device using graphene/polyaniline inks. *J Power Sources* **2014,** *248*, 483-488.

55. Ho, C. C.;   Murata, K.;   Steingart, D. A.;   Evans, J. W.; Wright, P. K., A super ink jet printed zinc–silver 3D microbattery. *Journal of Micromechanics and Microengineering* **2009,** *19* (9).

56. Wei, T. S.;   Ahn, B. Y.;   Grotto, J.; Lewis, J. A., 3D Printing of Customized Li-Ion Batteries with Thick Electrodes. *Adv Mater* **2018,** *30* (16), e1703027.

57. Fu, K.;   Wang, Y.;   Yan, C.;   Yao, Y.;   Chen, Y.;   Dai, J.;   Lacey, S.;   Wang, Y.;   Wan, J.;   Li, T.;   Wang, Z.;   Xu, Y.; Hu, L., Graphene Oxide-Based Electrode Inks for 3D-Printed Lithium-Ion Batteries. *Adv Mater* **2016,** *28* (13), 2587-94.

58. Hamel, M.; Mohellebi, H., A LabVIEW-based real-time acquisition system for crack detection in conductive materials. *Math Comput Simulat* **2020,** *167*, 381-388.

59.   H. A. Andrade, S. K., Software synthesis from dataflow models for G and LabVIEW. *Conference Record of Thirty-Second Asilomar Conference on Signals, Systems and Computers* **1998**.

60.   *Materials Data Book.* Cambridge University Engineering Department: 2003.

61.   Ltd., P. F., The seven sides of PTFE (or, why PTFE is way cooler than most realize). 2011.

62.   Pan, J.;   Xu, Y. Y.;   Yang, H.;   Dong, Z.;   Liu, H.; Xia, B. Y., Advanced Architectures and Relatives of Air Electrodes in Zn-Air Batteries. *Adv Sci (Weinh)* **2018,** *5* (4), 1700691.

63.   Ominde, N.;   Bartlett, N.;   Yang, X.-Q.; Qu, D., The effect of oxygen reduction on activated carbon electrodes loaded with manganese dioxide catalyst. *J Power Sources* **2008,** *185* (2), 747-753.

64.   Yu, G.;   Hu, L.;   Liu, N.;   Wang, H.;   Vosgueritchian, M.;   Yang, Y.;   Cui, Y.; Bao, Z., Enhancing the supercapacitor performance of graphene/MnO2 nanostructured electrodes by conductive wrapping. *Nano Lett* **2011,** *11* (10), 4438-42.

65.   Julien, C. M.; Mauger, A., Nanostructured MnO(2) as Electrode Materials for Energy Storage. *Nanomaterials (Basel)* **2017,** *7* (11).

66.   Wissler, M., Graphite and carbon powders for electrochemical applications. *J Power Sources* **2006,** *156* (2), 142-150.

67.   Corporation, N. I. NI USB-621x User Manual 2009.

68.   Company, C.-P. I. OPERATING MANUAL: L/S® DIGITAL PUMP DRIVES 2014.

69.   Hannifin, P. MPC SERIES PANEL MOUNT MASS FLOW CONTROLLER "INSTALLATION & PROGRAMMING" USER'S MANUAL

70.   Instruments, B.-L. S. Installation and   Configuration Manual for MPG-2xx series 2019.

CURRICULUM VITAE

Jingyu Si

PROFESSIONAL SUMMARY

Ph.D. in Mechanical Engineering with strong research and education professional experience for over seven years. One-year tier one electric vehicle industry professional experience. Focused fields include mechanical prototyping for electrochemical devices, battery system development and testing. A research team leader brings a combination of project management skills and research strategic planning. Current working with cell engineers to develop processes for evaluation of Lithium-ion cell using electrochemical approaches for electric vehicle.

PROFESSIONAL HIGHLIGHTS

- Highly motivated researcher with 7 + years' experience in long-duration battery system with automatic control development and testing.
- Successfully designed and fabricated advanced battery prototype with battery management system. Proficient with control algorithms for battery systems coding. Experienced with in C/C++, Python, LabVIEW and MATLAB.
- Actively involved in various projects like zinc-air flow battery, Lithium–sulfur battery, sodium/potassium- ion battery, ORR/OER electrocatalysts
- Experienced with materials analysis instruments including SEM/EDS, LC-MS, XRD, ICP-OES , Raman spectroscopy, TGA, BET and electrochemical analysis   instruments (Arbin), potentiostats (PARSTAT, Bio-Logic).
- Proficient with data management and statistical analysis software including Origin, MATLAB, Excel, Python.
- Provided coaching and guidance to a research team on a variety of experiments

Battery System Design | Electrochemistry | Test Protocols Development |Data Analysis | Data Interpretation | Experiment Strategic Planning | Team Leader

WORK EXPERIENCE

Battery Cell Engineering - *Rivian Automotive, LLC, Irvine, Ca*
September 2019 - PRESENT

- Design and setting up EIS automatic testing system for various temperatures (install and calibrate potentiostats (Bio-Logic), design cell fixture for cylinder Lithium-ion cell, build up and programming (LabVIEW) automatic testing system
- Processing various tests (shelf life test, cycling test, performance evaluation test) for different model of cylinder Lithium-ion cell
- Energy regeneration cell level benchmark test DOE design and process. (lifetime, degradation, max duration and power evolution for cells in various SOH)
- Battery module level thermal gradient data analysis.
- Cell level vehicle driving profile validation test. (power simulation)
- DFMEA for cylinder cell and cell level components.

Battery Cell Engineering Intern - *Rivian Automotive, LLC, Irvine, Ca*

May 2019 – Aug 2019
- Working with cell engineers to design protocols (PITT, GITT, EIS, CV) to extract modelling electrochemical parameters for cylinder Lithium-ion cell
- Setting up and testing massive cylinder cell test system (Abrin, BMS, temperature control system)
- Create a program to extract data from test result by python and MATLAB.
- Document SOPs for massive cylinder cell test system building up
- Coaching and guidance cell technician and new team member on a variety of experiments

Research team leader - *University of Wisconsin-Milwaukee, Milwaukee, WI*

September 2018 - May 2019

- Coordinated with lab manger to give safety training to new team members.
- Developed work schedules to match team members levels, monitored progress to improve work process efficiency.
- Mentored and coached team members in the design and execution of experiments.
- Definition and documentation of standard operating procedure.
- Overseen the setup of lab instrument prior to experiment for efficient and effective operation
- Performed personnel related activities such as hiring, scheduling, performance appraisals.
- Collected research data. Interpreted research data. Presented data findings.
- Guided and organized team members to present the project progress and results in research symposium

Class instructor - *University of Wisconsin-Milwaukee, Milwaukee, WI*

September 2018 – May 2019
- Taught courses weekly for up to 24 undergraduate engineering students (ME 101 Computational Tools for Engineers- MATLAB)
- Prepared materials and lessons to facilitate curriculum
- Provided relevant assignments for students that demonstrate learning outcomes in real problems of engineering
- Organized and guided students for final project
- Completed grade books learning assessments and final exam assessments on a timely basis

Research assistant for Energy Advancement Lab - *University of Wisconsin-Milwaukee, Milwaukee, WI*

January 2015 – September 2018
- Next generation metal-air batteries design and development

- Advance flow batteries design and development
- Research on fluidic electrode making and depth of discharge investigation.
- Study on making air electrode in various structure and components
- Fluidic systems control and monitor
- Control program (LabVIEW) for battery management writing and testing.
- Lithium–based batteries
- ORR/OER catalysts electrosynthesis
- Sodium/Potassium-Ion Batteries

Lab instructor - *University of Massachusetts Boston, Boston, MA*

September 2012 – December 2014

- Prepared and guide up to 32 students through experiment (CHEM 117Chemical Principles I Laboratory/ CHEM 118 Chemical Principles II Laboratory)
- Corrected laboratory reports to help students improve their scientific writing skills
- Assisted in proctoring and grading exams for general chemistry lectures

EDUCATION

Ph.D. Dissertator in Mechanical Engineering - *University of Wisconsin-Milwaukee, Milwaukee, WI*

Jan.2015- Aug.2020   GPA 3.667/4.00

Master of Science in Chemistry - *University of Massachusetts Boston, Boston, MA*

Sep. 2012 – Dec. 2014

Bachelor of Engineering in Chemical Engineering   **-** *Tianjin University of Science and Technology, Tianjin, China*

Sep. 2007 - May 2011

PROFESSIONAL SKILLS

- **Programming and Computer Science:** Proficient with LabVIEW, C, MATLAB. Python and 2D/3D CAD tools.
- **Data analysis and graphing:**   Proficient with Origin, MATLAB, Excel.
- **Lab Research Skills:**

- ✓ Mechanical prototype design and fabrication
- ✓ Battery system building and testing
- ✓ Battery management system algorithm design and coding (LabVIEW)
- ✓ Electrochemical Impedance Spectroscopy
- ✓ Battery Test Equipment (Arbin)
- ✓ Potentiostats (PARSTAT, Bio-Logic)
- ✓ SEM/EDS
- ✓ LC-MS
- ✓ XRD
- ✓ ICP-OES
- ✓ Raman spectroscopy
- ✓ TGA
- ✓ BET
- ✓ Viscometer
- ✓ 3D Printin
- ✓
- Excellent communication skills with a focus on team-building
- Outstanding organizational, multitasking, and problem-solving abilities.

AWARDS AND HONORS

CHANCELLOR'S AWARD - *University of Wisconsin-Milwaukee*

2017

Departmental Awards of Student Research Poster Competition - *University of Wisconsin-Milwaukee*

2019

PROFESSIONAL MEMBERSHIPS

- The Electrochemical Society (August 2018 – present)

LANGUAGE COMPETENCIES

- English: fluent (speaking, reading, writing)
- Mandarin: native language

PUBLICATIONS & PRESENTATIONS

Investigation of the Li–S Battery Mechanism by Real-Time Monitoring of the Changes of Sulfur and Polysulfide Species during the Discharge and Charge

Dong Zheng†, Dan Liu‡, Joshua B. Harris†, Tianyao Ding†, **Jingyu Si**†, Sergei Andrew†, Deyu Qu‡, Xiao-Qing Yang§, and Deyang Qu*†

September 2016   ACS Appl. Mater. Interfaces

Highly Efficient Ni-Fe Based Oxygen Evolution Catalyst Prepared by A Novel Pulse Electrochemical Approach

Gongwei Wang, Dong Zheng ,Dan Liu, Joshua Harris, **Jingyu Si,** Tianyao Ding, Deyang Qu

September 2017 Electrochimica Acta

The Design and Investigation Zinc-Air Flow Battery with Automatic Control System (Poster Presentation)

J. Si, D. Zheng, G. Wang, D. Liu, J. Harris, and D. Qu

May 2017   The Electrochemical Society

The Progress of Li–S Batteries—Understanding of the Sulfur Redox Mechanism: Dissolved Polysulfide Ions in the Electrolytes

Dong Zheng   Gongwei Wang   Dan Liu   **Jingyu Si**   Tianyao Ding   Deyu Qu   Xiaoqing Yang Deyang Qu

June 2018   Advanced Materials Technologies

Systematic and rapid screening for the redox shuttle inhibitors in lithium-sulfur batteries

Dong Zheng, Gongwei Wang, Dan Liu, Joshua B.Harrisa,   Tianyao Ding, **Jingyu Si**, Deyu Qu, Xiao-Qing Yang, Deyang Qu

June 2018 Electrochimica Acta

Confined Phosphorus in Carbon Nanotube-Backboned Mesoporous Carbon as Superior Anode Material for Sodium/Potassium-Ion Batteries

Dan Liu, Xingkang Huang, Deyu Qu, Dong Zheng, Gongwei Wang, Joshua Harris, **Jingyu Si**, Tianyao Ding, Junhong Chen, Deyang Qu

July 2018   Nano Energy